



HAL
open science

Sea surface temperature impact on diurnal cycle and seasonal evolution of the Guinea Coast Rainfall in boreal spring and summer

Manuel Tanguy, Gaëlle de Coëtlogon, Laurence Eymard

► To cite this version:

Manuel Tanguy, Gaëlle de Coëtlogon, Laurence Eymard. Sea surface temperature impact on diurnal cycle and seasonal evolution of the Guinea Coast Rainfall in boreal spring and summer. *Monthly Weather Review*, 2022, 150 (12), pp.3175-3194. 10.1175/MWR-D-21-0155.1 . insu-03542344v2

HAL Id: insu-03542344

<https://insu.hal.science/insu-03542344v2>

Submitted on 21 Dec 2022

HAL is a multi-disciplinary open access archive for the deposit and dissemination of scientific research documents, whether they are published or not. The documents may come from teaching and research institutions in France or abroad, or from public or private research centers.

L'archive ouverte pluridisciplinaire **HAL**, est destinée au dépôt et à la diffusion de documents scientifiques de niveau recherche, publiés ou non, émanant des établissements d'enseignement et de recherche français ou étrangers, des laboratoires publics ou privés.

Sea Surface Temperature Impact on Diurnal Cycle and Seasonal Evolution of the Guinea Coast Rainfall in Boreal Spring and Summer

MANUEL TANGUY,^a GAËLLE DE COËTLOGON,^a AND LAURENCE EYMARD^a

^a *LATMOS-IPSL, Sorbonne Université, Paris, France*

(Manuscript received 8 July 2021, in final form 17 November 2021)

ABSTRACT: ERA5 reanalyses and observations of convective clouds and precipitation are used over the northern Gulf of Guinea between 7°W and 3°E to study the influence of ocean surface temperature and the land–sea temperature gradient on Guinea Coast rainfall (GCR) in boreal spring and summer. Seasonal composites are calculated around two dates indexing the onset (T_{ref}) and demise (T_{end}) of the GCR. The T_{ref} date corresponds to the emergence of the equatorial upwelling in boreal spring, which “pushes” the zonal precipitation belt northward against the Guinea coast. The T_{end} date characterizes the emergence of the coastal upwelling in July, which is known to coincide with the beginning of the “Little Dry Season” that lasts until September. Along the Guinea Coast, the diurnal cycle of the air–sea temperature gradient controls precipitation through the land–sea breeze, which explains why precipitation reaches its maximum around noon over the ocean, and in the late afternoon over the continent. The emergence of the Guinea Coast upwelling in July induces a weakening of southerlies on a seasonal scale, and a weaker land breeze on a diurnal scale. It induces a decrease in the convergence of humidity transport across the coast and in coastal oceanic precipitation. Therefore, the GCR is seasonally controlled by the latitude of the maximum tropospheric water vapor content and the annual cycle of the West African monsoon, but the ocean surface temperature is responsible for the abruptness of its onset via the intensification of the equatorial upwelling around the end of May, and possibly of its demise as well via the emergence of the coastal upwelling by early July.

KEYWORDS: Diurnal effects; Monsoons; Sea breezes

1. Introduction

The correct representation of precipitation in numerical atmospheric models remains one of the most important challenges in climate physics (IPCC 2007; Bony et al. 2015), particularly in West Africa, where precipitation is poorly represented in models (Sylla et al. 2013; Roehrig et al. 2013; Harlaß et al. 2015; Steinig et al. 2018; Kniffka et al. 2020; Sow et al. 2020; Kouadio et al. 2020). A better understanding of processes controlling precipitation is therefore needed in order to improve its representation.

Precipitation in West Africa is primarily controlled by the monsoon, driven by a huge meridional contrast in temperature and humidity between eastern tropical Atlantic and the dry continent farther north (Parker et al. 2017). In response to the annual solar cycle, precipitation latitude exhibits a strong seasonal cycle (Peyrillé et al. 2007; Hagos and Cook 2007; Thorncroft et al. 2011; Maranan et al. 2018). The zonal band of precipitation is centered on the northern Gulf of Guinea and Guinea Coast (around 5°N) between late April and early July (see Fig. 1 for May and June precipitation). This near-coastal oceanic precipitation, named the Guinea Coast rainfall (GCR; Nguyen et al. 2011), shifts northward in late June/early July and brings precipitation over the Sahel

(see Fig. 1 for July precipitation) until September, during the monsoon demise, when the Guinea Coast countries experience a second rainfall peaking in October–November (Sultan and Janicot 2003; Zhang and Cook 2014). Between July and September, precipitation over the coastal region is scarce between 12°W and 7°E and is referred to as the “Little Dry Season” (Adejuwon and Odekunle 2006; Fink et al. 2017; Wainwright et al. 2019). Precipitation is mainly localized over the ocean during the rest of the year. The countries along the northern coast of the Gulf of Guinea therefore experience two rainy seasons and two dry seasons per year; the near-coastal precipitation in June/early July is of particular interest, because it may condition the onset of summer monsoon in the Sahel through the control of the meridional gradient of soil moisture (Zheng et al. 1999). Furthermore, its interannual variability has been shown to be largely controlled by sea surface temperature (SST) in the eastern Tropical Atlantic (Giannini et al. 2003; Polo et al. 2008; Losada et al. 2010; Suárez-Moreno et al. 2018). However, few previous studies have conducted a thorough investigation of the mechanisms linking SST and the onset or demise of GCR on intraseasonal time scales.

The northward migration of the zonal band of precipitation, also known as the “monsoon jump” around 24 June (Sultan and Janicot 2003), and the variability of precipitation in boreal summer, have been extensively studied in the international

 Denotes content that is immediately available upon publication as open access.

Corresponding author: Manuel Tanguy, manuel.tanguy@latmos.ipsl.fr

Publisher's Note: This article was revised on 16 December 2022 to replace the hard-to-read version of Fig. 2 that was originally published.

DOI: 10.1175/MWR-D-21-0155.1

© 2022 American Meteorological Society. For information regarding reuse of this content and general copyright information, consult the [AMS Copyright Policy](#) (www.ametsoc.org/PUBSReuseLicenses).

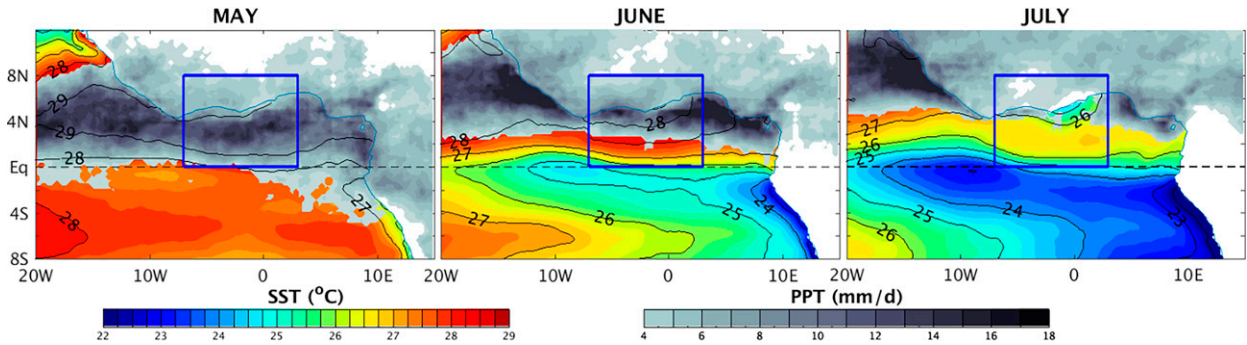


FIG. 1. 2008–15 SST (Reynolds product; color shading and black contours from 24° to 27°C, intervals of 1°C) and precipitation larger than 4 mm day⁻¹ (TRMM, gray shading) in (left) May, (center) June, and (right) July. The blue frame delimits the region of scrutiny, and the black dashed line indicates the equator.

African Monsoon Multidisciplinary Analysis (AMMA) project (Redelsperger et al. 2006) and shown to be primarily controlled by the continental surface (Wang and Eltahir 2000; Thorncroft et al. 2011). However, precipitation is also controlled by SST in the Gulf of Guinea, where a strong equatorial upwelling emerges in boreal spring and summer (see blue bands in June and July, in Fig. 2), increasing meridional thermal gradients at the surface (Okumura and Xie 2004; Caniaux et al. 2011; Nguyen et al. 2011; Nnamchi and Li

2011; Leduc-Leballeur et al. 2013; Crespo et al. 2019; Worou et al. 2020). Using numerical simulations, Meynadier et al. (2015) showed that the emergence of equatorial upwelling controls the GCR onset in late May, through an increase in surface winds north of the equator and a convergence of humidity near the Guinea Coast, represented by monsoon flow and coastal convergence increases in Fig. 2. In addition, a strong coastal upwelling appears along the Guinea Coast in boreal summer (July–September), where the SST decreases from about 30°C in May to 24°–25°C in August (Odekunle and Eludoyin 2008; Ali et al. 2011; Kouadio et al. 2013). It is composed of two parts: west of Cape Three Points off Ivory Coast, and farther east, off Ghana, Togo, and Benin, and both parts are surrounded by the eastward Guinea Current (Odekunle and Eludoyin 2008). The dynamics of the Guinea coast upwelling remains poorly understood; however, Djakouré et al. (2017) performed idealized numerical experiments and found that while the coastal upwelling west of Cape Three Points is highly sensitive to the inertia and detachment of the Guinea Current from the coast, the upwelling east of Cape Three Points is primarily induced by local winds through the divergence of the Ekman transport. Ali et al. (2011) found strong correlations between GCR variability and equatorial and coastal upwellings, and Bakun (1978) observed a significant reduction in precipitation along the coast where coastal upwelling is strongest. Other studies have suggested an influence of Guinea Coast upwelling on nearby continental precipitation (Gu and Adler 2004; Kouadio et al. 2013; Nnamchi and Li 2011; Aman et al. 2018). SST in the Gulf of Guinea, particularly in the equatorial and coastal upwelling areas, could therefore influence the GCR demise as well as its onset, in particular via the modification of meridional land–sea temperature gradient as suggested by Thorncroft et al. (2011); but to our knowledge, no studies have yet examined the involved mechanisms.

In addition to the seasonal cycle, the land–sea temperature gradient also exhibits a strong diurnal cycle (Sultan et al. 2007) related to land–sea-breeze regimes (Gambie and Steyn 2013; Abayomi et al. 2007; Parker et al. 2017; Guedje et al. 2019; Coulibaly et al. 2019). The land–sea-breeze strength is maximum in boreal winter, but a second maximum is found in May, before reaching an annual minimum in July–August

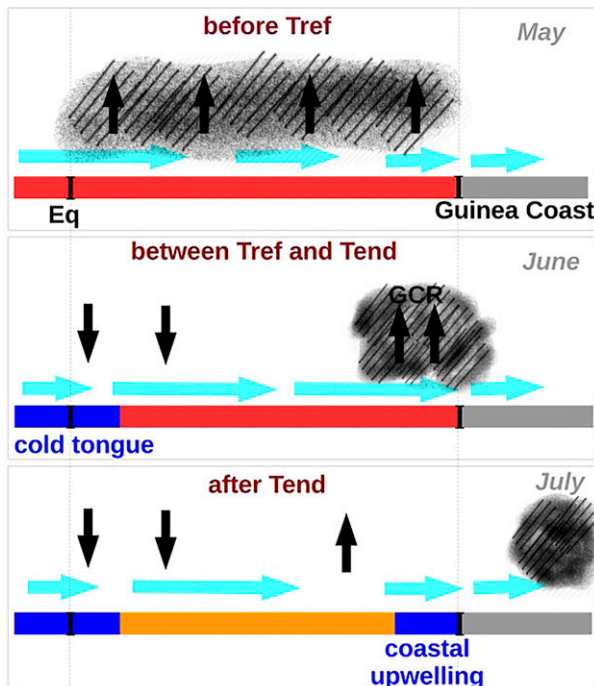


FIG. 2. Scheme of the SST influence on precipitation through low-level convergence between the equator and the Guinea Coast from before T_{ref} to after T_{end} : monsoon flow (light blue horizontal arrows), low-level convergence (black upward arrows) or divergence (black downward arrows), and resulting precipitation (black hatches). May, June, and July tags are not specific but rough indicators.

(Guedje et al. 2019; Coulibaly et al. 2019); its interaction with the monsoon flow could therefore impact the GCR variability. In particular, land–sea breeze has a strong impact on the atmospheric boundary layer at diurnal time scale, through the triggering of convection (Flamant et al. 2018; Knippertz et al. 2017; Parker et al. 2017). Therefore, a thorough study of the GCR needs to be done at diurnal time scales.

The SST influence on the GCR onset has already been investigated in previous studies over the decade of the 2000s (Leduc-Leballeur et al. 2013; Meynadier et al. 2015). The present work extends this study to the whole GCR period between 2008 and 2015, and in addition, the influence of the coastal upwelling on the end of the GCR is investigated. Recently available data with an hourly resolution allow us to study the impact of the land–sea surface temperature gradient on the precipitation at diurnal time scales. Reanalyses from the European Centre for Medium-Range Weather Forecasts (ERA5) and satellite observations of clouds and precipitation are used to examine the links between surface temperature, low-level atmospheric convergence and precipitation at seasonal and diurnal time scales. Low-level convergence is indeed known to be strongly connected with precipitation: Weller et al. (2017) found that between 65% and 90% of the precipitation is associated with long coherent lines of low-level convergence over the global oceans, against 30%–60% over land. It is therefore interesting to investigate if low-level convergence could be controlled by the surface temperature gradients in the Gulf of Guinea, and what impact it could have on the GCR, in particular on its onset and demise.

The second section describes the different datasets. Section 3 investigates the GCR onset and confirms that previous results are found again with these new data. Section 4 investigates the GCR at diurnal time scales. Section 5 presents an estimate of the GCR demise date using a surface temperature index in the core of the coastal upwelling and composites computed around this date. A summary and conclusion are presented in section 6.

2. Data and method

Cloud types are extracted from SAFNWC cloud type product, using an algorithm (Derrien and Gléau 2005, 2010) developed for measurements of the Spinning Enhanced Visible and InfraRed Imager (SEVIRI). This instrument onboard the Meteosat Second Generation (MSG) is an optical imaging radiometer including 12 different spectral channels in the visible and infrared range with a 1–3-km spatial resolution and a 15-min temporal sampling. For each 3-km pixel, the cloud presence (1) or absence (0) in each of the 21 different classes is indicated. From these 21 classes available in the database, we merge “low” (class 6) and “ultra low clouds” (class 8) in a mixed class called hereafter “low clouds.” We also gather “thick high clouds” (class 12) and “very thick high clouds” (class 14) in a mixed class called “probable deep convective clouds.” To keep the dataset easy to use, and for comparison with others, a reduced grid mesh ($0.25^\circ \times 0.25^\circ \times 1$ h) is used. In each grid mesh the probability of occurrence of clouds in each cloud class is calculated, as well as the associated spatial variance.

Precipitation intensity is provided by mission level 3 product 3B42V7 (TRMM) (Huffman et al. 2007). It has been derived primarily from the TRMM mission until 2014, and is a multimission product (microwave and infrared radiometers), before it was recently stopped.¹ Product resolution is $0.25^\circ \times 0.25^\circ$, every 3 h. Precipitation is transformed into an event occurrence by summing the events with a quantity greater than 0.1 mm h^{-1} to limit the quantitative bias known to exist with parameterized convection. Akinsanola et al. (2017) showed that TRMM was one of precipitation datasets that can be used for precipitation assessment over West Africa.

ERA5 ECMWF reanalysis was generated using the four-dimensional variational analysis system (Copernicus Climate Change Service 2017; Hersbach et al. 2020). Data were extracted at 27 levels from 1000 to 100 hPa with a 0.25° horizontal resolution. The parameterization of the convection scheme has been changed since the previous version of reanalyses (ERA-Interim) by adding a convective available potential energy (CAPE) closure based on the work presented in Bechtold et al. (2014), which showed a better representation of the diurnal cycle. Analysis variables (wind, relative humidity, temperature, total column water vapor) are retrieved at a 6-h resolution (0000, 0600, 1200, and 1800 UTC). Precipitation is the addition of shallow, large-scale, and convective rainfalls in forecast variables, and is retrieved at an hourly time step from the +6- to +18-h forecasts, twice a day. Surface fields as 10-m surface wind and skin temperature (SKT) is also retrieved at an hourly resolution. The surface parameterization scheme computes SKT in two different ways, whether on the ocean or on the continent. On the ocean, the SKT product is based on a model simulation with data from satellite-derived SST (Hersbach et al. 2020), which is quite close to the SKT, with a small bias of less than 0.3°C and a similar variability (not shown). In spite of a significant improvement from the previous ECMWF reanalysis (ERA-Interim), the continental SKT in ERA5 is still not very reliable (Johannsen et al. 2019), especially in southern West Africa (Flamant et al. (2018), see in particular their Fig. S6). However, SKT (and not SST) is considered here in the coastal region of southern West Africa because it makes possible to compute the surface temperature gradient between the continent and the sea at diurnal time scale. The difference between SKT and SST is rather small, the SKT is colder than the SST of up to 0.2°C between 1° and 3°N (not shown). It is also notable that this difference is minimal and almost zero near the coast, when the coastal upwelling appears in July. The 10-m wind is very close from the assimilated satellite product (ASCAT during 2008–15) and is weakly biased in the region under scrutiny (see Fig. A1 in the appendix). Part of the infrared measurements used in TRMM precipitations are also assimilated in this reanalysis. These data were provided by the Copernicus Climate Change Service and made available by the IPSL/ESPRI mesocenter: <https://confluence.ecmwf.int/display/CKB/ERA5%3A+data+documentation>

Results presented in this study are mainly based on ERA5, but three additional reanalyses are also investigated:

¹ <https://pmm.nasa.gov/data-access/downloads/TRMM>.

- MERRA-2: a $0.5^\circ \times 0.625^\circ$ hourly reanalysis produced by NASA's Global Modeling and Assimilation Office (Gelaro et al. 2017) with version 5.12.4 of the Geostationary Operational Environmental Satellites atmospheric data assimilation system. To deal with the difficulty of maintaining a realistic balance between total mass and total water vapor, sources and sinks of atmospheric water have been added to the model continuity equation so that changes in total mass are driven by changes in total water. MERRA-2 products are accessible online through the NASA Goddard Earth Sciences Data Information Services Center (GES DISC).
- Climate Forecast System Reanalysis [hereafter CFSR; Saha et al. (2014)]: A global, high resolution, coupled atmosphere–ocean–land surface–sea ice system including coupling of atmosphere and ocean during the generation of the 6-h guess field, with an atmosphere resolution of about 38 km (T382) with 64 levels.
- JRA-55 (hereafter JRA) is a $0.5^\circ \times 0.5^\circ$ 3-hourly atmospheric reanalysis produced by the Japan Meteorological Agency (Kobayashi et al. 2015), with a TL319 global spectral model using a conservative semi-Lagrangian scheme in which vertically advection is processed separately from horizontal advection (so that the model may preserve the conservation of vertically integrated quantities, such as water vapor, under non-dissipative conditions).

The data used hereafter are 3- and 6-h forecasts based on analysis with a 6-h time step. The following observational datasets of SST and surface wind are also retrieved at the daily scale:

- High-resolution Reynolds SST product developed using optimum interpolation, the Advanced Very High Resolution Radiometer (AVHRR) infrared satellite SST data and in situ data from ships and buoys (Reynolds et al. 2007), retrieved from the NOAA NCDC website,² with a spatial grid resolution of 0.25° . The difference between this observed SST and the SKT ERA5 (see Fig. A1) shows two regions where the biases are maximum: between the equator and 2N, with a cold bias in ERA5 SKT of 0.4°C in May that increases up to 0.7°C after the emergence of equatorial upwelling and a second bias close to the coast, cold and rather weak in May and June (0.1°C) which become a warm bias of about 0.2°C in July with the development of coastal upwelling.
- ASCAT ocean surface winds, or 10-m neutral stability wind, obtained from the following website: <https://manati.star.nesdis.noaa.gov/datasets/ASCATData.php>. The latter product, processed by the NOAA, is derived from scatterometer measurements of Advanced Scatterometer (ASCAT), aboard EUMETSAT Meteorological Operational (METOP) satellite. The geophysical model function (GMF) is CMOD5.5: It relates the normalized radar cross section to the ocean surface wind speed and direction. The original grid resolution is 0.25° and data are available at daily time scale.

The present study focuses on the southern coastal region of West Africa, extending from Ivory Coast to Benin

between 7°W and 3°E , and from May to July 2008–15 (blue frame in Fig. 1). Results showing vertical circulation maps or time/latitude diagrams are based on averages computed between 1°W and 1°E , in order to accurately monitor hourly events in the diurnal cycles presented in sections 3 and 4, and in section 2 for simplicity and consistency between the different plots. Taking a different longitude band (five bands of 2° , from $5^\circ\text{--}3^\circ\text{W}$ to $3^\circ\text{--}5^\circ\text{E}$, were tested) only slightly changed the results and left the conclusions of this study unchanged.

3. Onset of the Guinea Coast rainfall

Figure 1 shows a monthly climatology of SST (color shading and black contours) and precipitation (gray shading) in ERA5, from May to July between 2008 and 2015 in the eastern tropical Atlantic. In May, a zonal band of intense precipitation extends between the Equator and the Guinea Coast, with a maximum around 3N (Fig. 1a). In June, the zonal band settles just south of the Guinea Coast, with values greater than 8 mm day^{-1} confined north of $3^\circ\text{--}4^\circ\text{N}$ in the region $0^\circ\text{--}8^\circ\text{N}$, $7^\circ\text{W--}3^\circ\text{E}$ (blue frame, Fig. 1b). Between May and June, the emergence of the equatorial upwelling induces a strong positive SST gradient of about $2^\circ\text{--}3^\circ\text{C}$ around its northern front (roughly at 1°N), which persists until July despite a general cooling of the SST: Meynadier et al. (2015) showed that this front intensification forces the GCR onset by increasing the atmospheric pressure gradient across the front, which strengthens the southerlies toward the Guinea Coast.

The Atlantic equatorial upwelling is known to exhibit very large interannual variability regarding its date of emergence and intensity (Marin et al. 2009; Caniaux et al. 2011), and so is the GCR (Worou et al. 2020). Moreover, precipitation data is very scattered and not normally distributed (see Fig. A2 in the appendix): a date of the GCR onset based on precipitation is therefore very difficult to define objectively. On the other hand, previous studies have identified an abrupt change in the surface wind pattern associated with the equatorial upwelling emergence, when southerlies between the equator and the coast become stronger than south of the equator in the equatorial upwelling (also known as the Atlantic cold tongue) region (Leduc-Leballeur et al. 2013; Meynadier et al. 2015). The date of the GCR onset, hereafter T_{ref} , is computed by following this method: it is defined as the day when southerlies averaged in the box $3^\circ\text{W--}5^\circ\text{E}$, $1^\circ\text{--}4.5^\circ\text{N}$ (north of the front) become, and remain, stronger than in the box $3^\circ\text{W--}5^\circ\text{E}$, $4^\circ\text{S--}0^\circ$ (south of the front) for the remaining of the season. Using 2000–09 QuikSCAT surface wind, previous studies found that T_{ref} occurred after 12 May and before 25 June, with an average on 30 May (Leduc-Leballeur et al. 2013). In the present study, using 2008–15 ASCAT meridional surface wind, its range is 16 May–6 June with an average on 27 May. Note that (Sultan and Janicot 2003) estimated a date of monsoon preonset by taking the day when the westward zonal wind averaged between 10°W and 10°E turns eastward at 15°N (i.e., going from negative to positive values): they found 14 May on average (plus or minus a root-mean-square of 9.5 days).

Two composites of ERA5 surface wind divergence and MSG cloud cover were computed around T_{ref} . The first is an

² <http://www.esrl.noaa.gov/psd/>.

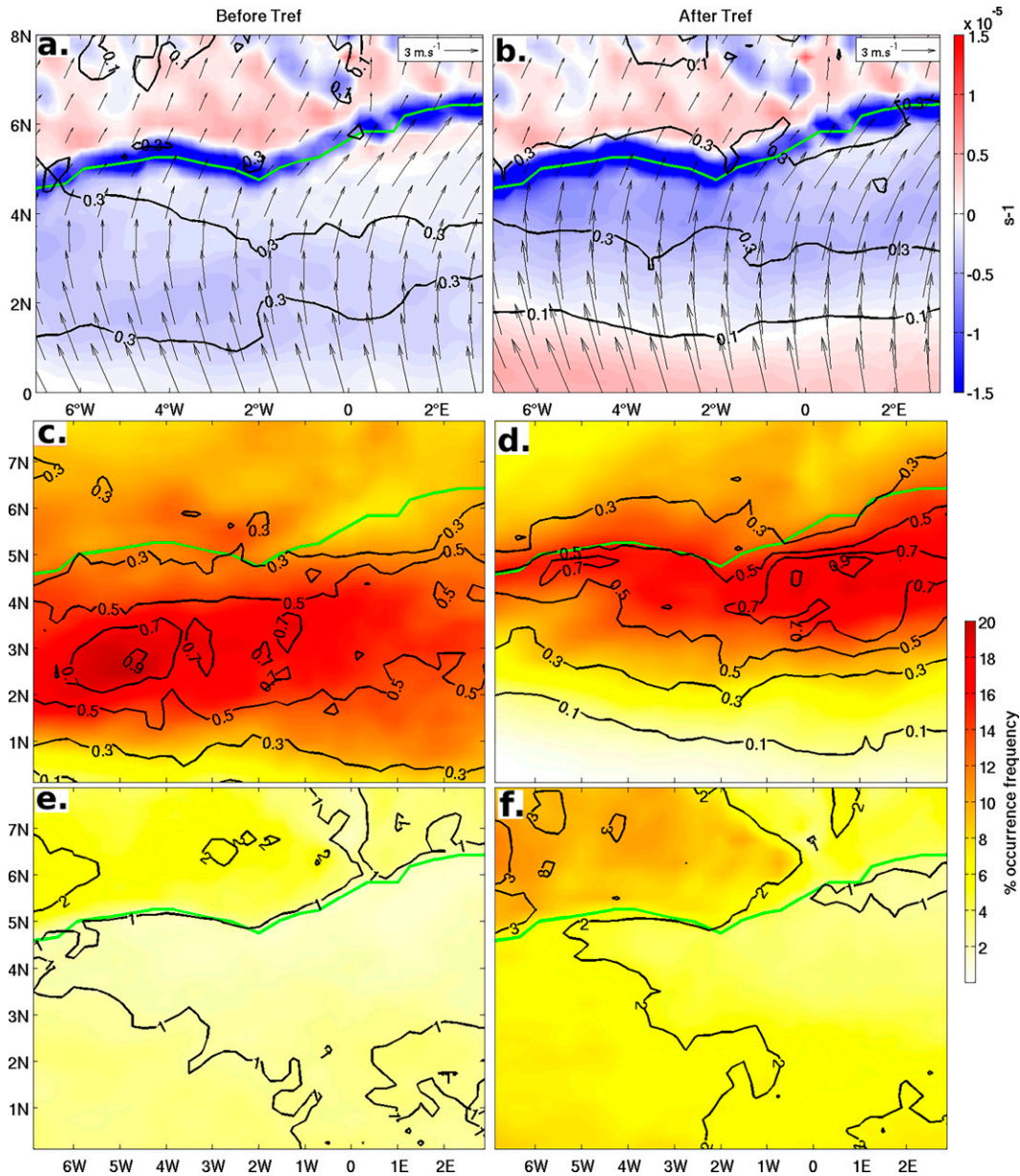


FIG. 3. Composites of 14 days (left) before and (right) after T_{ref} : (a),(b) ERA5 surface wind (black arrows), surface wind divergence (s^{-1} ; shading), and precipitation (black contours; mm h^{-1}). (c),(d) MSG convective clouds (shading) and TRMM precipitation (black contours; mm h^{-1}). (e),(f) MSG low clouds (shading) and their spatial variance (black contours). The green line stands for the coastline.

average over 2008–15 of the two weeks preceding T_{ref} (i.e., between T_{ref} minus 14 days and T_{ref} , Fig. 3, left column), and the second of the two weeks following T_{ref} (between T_{ref} and T_{ref} plus 14 days, Fig. 3, right column). Weak surface convergence is found throughout the Gulf of Guinea before T_{ref} , except along the Guinea Coast where surface wind is strongly convergent (Fig. 3a): Surface wind decreases a lot when it encounters the continent, mainly because of a much larger friction over the land than over the ocean which deepens the boundary layer through induced turbulence. In addition, a warmer

continental surface could also contribute to the boundary layer deepening and weakening of surface wind over the continent, but the implied surface heat flux is clearly dominated by the strong diurnal cycle of the continental surface temperature, which is investigated in the next section. Convective clouds are frequent (10%–20% of the time) between the equator and the coast (at 5°–6°N), with a maximum around 2°–3°N (Fig. 3c, shading). The precipitation is scattered over the ocean, with a maximum around 2°–3°N, in observations (Fig. 3c, black contours) as well as in ERA5 (Fig. 3a, black

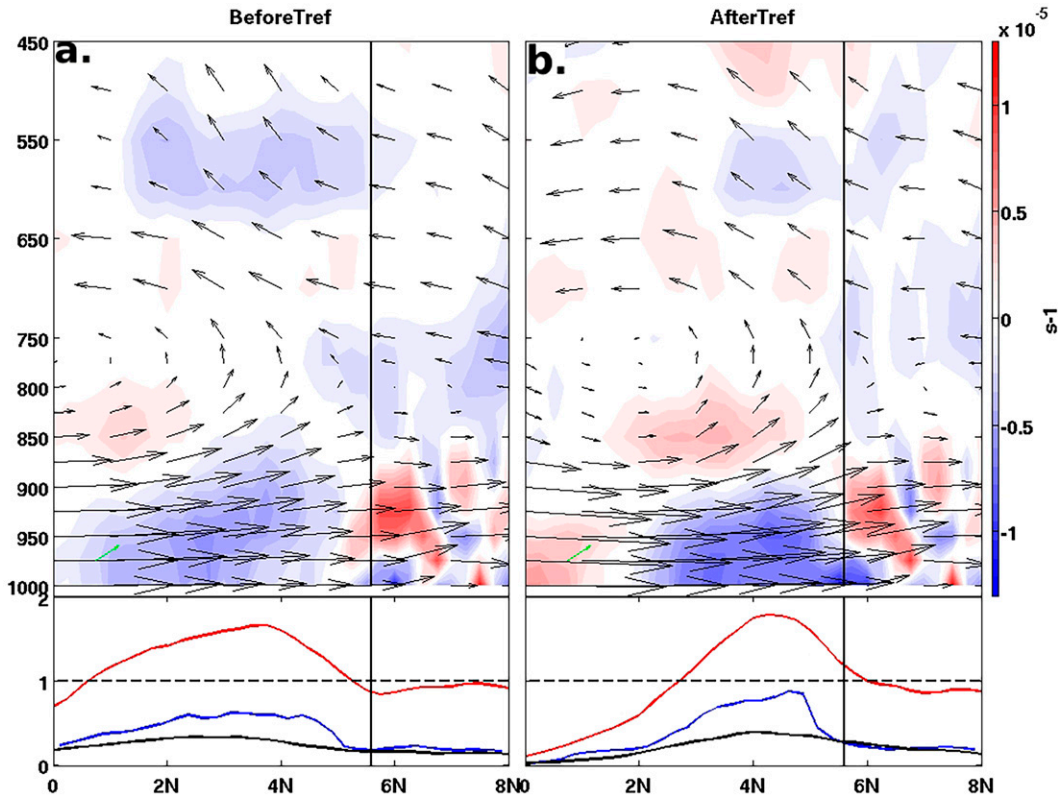


FIG. 4. Composites of 14 days (a) before and (b) after T_{ref} , 1°W – 1°E : ERA5 horizontal wind divergence (shading) and meridional circulation (black arrows) and MSG convective cloud occurrence frequency ($\times 10\%$; red line) and precipitation (ERA5 in black line, TRMM in blue line; mm h^{-1}).

contours), although they are about twice as low in the latter. Low clouds are generally scarce (less than 5% of the time), with a maximum found on the continent, west of 1°W (Fig. 3e).

After T_{ref} , the surface wind strengthens in the Gulf of Guinea, mostly driven by the meridional SST gradient across the northern front of the equatorial upwelling: when the latter intensifies, it increases the magnitude of the atmospheric pressure gradient across the front through hydrostatic balance (not shown), which strengthens surface wind from the cold to the warm side of the front (Lindzen and Nigam 1987). A meridional gradient of SST therefore induces a wind divergence when the gradient is positive along the mean wind direction, and a convergence when it is negative (Chelton et al 2001, 2004). Furthermore, previous studies showed that the warming of the sea surface temperature decreases vertical atmospheric stability, thereby increasing vertical turbulent flux of horizontal momentum from stronger winds aloft: this also tends to strengthen the surface wind blowing from cold to warm areas within a few minutes or hours (Sweet et al. 1981; Wallace et al. 1989; Hayes et al. 1989). As a result, over the cold tongue and its northern front, a strong divergence of surface wind is found south of 3°N after T_{ref} , which tends to inhibit deep atmospheric convection and precipitation, while between 3°N and the Guinea Coast an increased convergence against the Guinea Coast maximizes precipitation (Fig. 3b).

The T_{ref} seasonal transition is also clearly visible in both convective clouds (Fig. 3d, shading) and low clouds occurrence (Fig. 3f), as well as in TRMM precipitation (Fig. 3d, black contours): A northward shift of convective clouds toward the coast is clearly observed, with a maximal occurrence of 15%–20% in a zonal band between 3° and 6°N , in good agreement with the northward shift of convergence seen in ERA5 (Fig. 3b). South of 3°N , low clouds, which include both stratiform and shallow cumuliform clouds, become more frequent (Fig. 3f), probably in response to the increase of surface wind divergence. Indeed, subsidence over cold areas in eastern tropical oceans enhances the temperature inversion capping the marine boundary layer, which favors the formation of low-level stratus (Myers and Norris 2013). Eventually, observed precipitation maximum is in very good agreement with the location of convective clouds (Figs. 3c,d). This good match confirms that the chosen cloud class is a very good proxy for monitoring deep convection.

Figure 4 shows composites of vertical meridional circulation in ERA5 between 1°W and 1°E around T_{ref} , allowing us to observe the vertical extension of the divergence/convergence dipole patterns observed at the surface. Below each cross section, precipitation in ERA5 (black) and TRMM (blue), and MSG convective cloud occurrence (red) are also plotted. Before T_{ref} , the strong northward monsoon flow is observed below 850 hPa, with an overlying southward and partially converging flow above 750 hPa (Fig. 4a). This return flow subsides

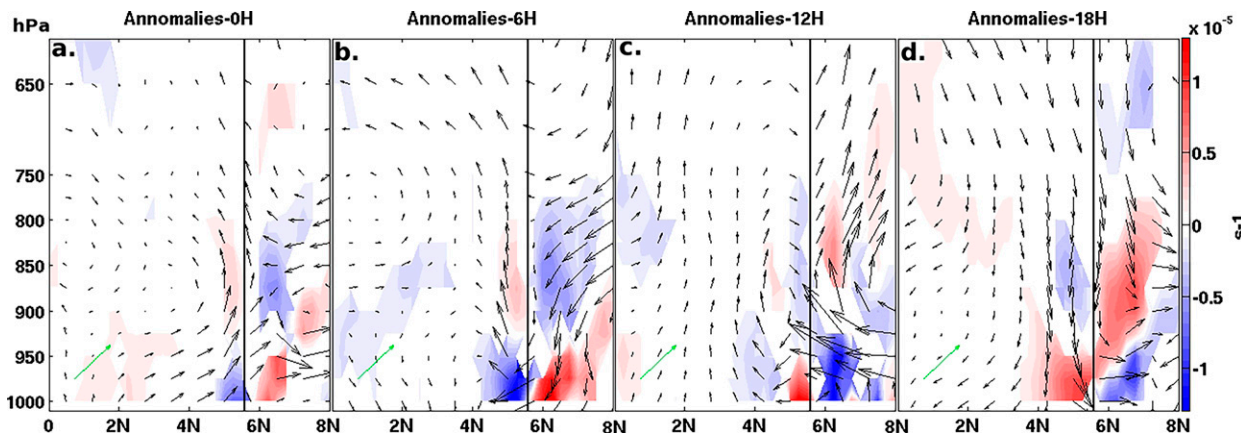


FIG. 5. Diurnal composites of 14 days after T_{ref} , 1°E – 1°W : ERA5 diurnal anomalies of meridional circulation (black arrows) and horizontal divergence (shading; s^{-1}) at (a) 0, (b) 6, (c) 12, and (d) 18 h. The green arrow stands for 1 m s^{-1} horizontally and -1 hPa s^{-1} vertically.

south of 2S , driven by the South Atlantic high pressure (not seen in the figure). After T_{ref} , as discussed previously, the wind is weaker south of the equator and stronger farther north, inducing a surface divergence and a low-level subsidence south of 2°N , while surface convergence and convection have increased toward the coast (Fig. 4b). Precipitation in ERA5 matches this change in low-level divergence: before T_{ref} , values are maximum around 2° – 3°N (Fig. 4a, black profile); after T_{ref} , they decrease (increase) south (north) of 3°N (Fig. 4b), following the reinforcement of the low-level divergence south of 3°N and convergence between 3°N and the Guinea Coast.

As expected from horizontal maps seen in Fig. 3, very similar evolution from before to after T_{ref} is found in observed precipitation (Fig. 4, blue profiles), but with a larger decrease south of 3°N and a larger increase between 3°N and the Guinea Coast, and with a peak of nearly 1 mm h^{-1} observed just south of the coast after T_{ref} . It is clear that, in spite of a huge improvement of the representation of precipitation in ERA5 compared to previous reanalyses, as for example documented for intraseasonal to interannual time scales in East Africa (Gleixner et al. 2020), the ERA5 reanalysis represents only about half of the observed precipitation intensity between 3°N and the Guinea Coast. We suggest that this bias could come from a negative bias in ERA5 surface southerlies compared to the observations, between the equator and the Guinea Coast (see Fig. A1): They are indeed too weak by 0.5 to 1 m s^{-1} , which may appear as a relatively small difference, but which implies a convergence near the coast after T_{ref} much more important in the observations than in ERA5 (cf. Figs. 3a,b and A3a,b), which could partly explain the too scarce precipitation in ERA5 (the other possibility being obviously a flaw in the parameterization of the deep atmospheric convection in ERA5, as in all global atmospheric models).

In summary, the dynamics of the low-level atmosphere in ERA5 corresponds to the pattern of convergence of surface winds and precipitation, with divergence tending to inhibit deep convection and precipitation south of 3° , and convergence tending to favor them north of 3° after T_{ref} . As already

explained, these changes can be attributed to changes in surface temperature, in particular to the intensification of the northern front of the cold tongue (Fig. 1b): Following a similar reasoning, the development of the coastal upwelling along the Guinea Coast in July could play a role in the disappearance of the GCR (Fig. 1c). But before investigating this issue, as it leads the study closer to the continent, the diurnal cycle becomes important and is first examined in the next section.

4. Diurnal cycle of the Guinea Coast rainfall

Diurnal anomalies of the vertical meridional atmospheric circulation during the GCR season are computed by subtracting the zonal/vertical wind composite averaged over the two weeks lagging T_{ref} in 2008–15 between 1°W and 1°E (shown in Fig. 4b) from similar composites computed at 0, 6, 12, or 18 h (Fig. 5). Note that diurnal anomalies of surface wind speed anomalies do not exceed $\pm 0.5 \text{ m s}^{-1}$ within the day on either side of the coast (not shown), against more than 3 or 4 m s^{-1} on average for the seasonal composite: the strong southern monsoon flow below 850 hPa is clearly larger than any diurnal wind variability.

However, some diurnal anomalies of the wind divergence are found to be as large as seasonal values: for example, low-level anomalies of about $-1 \times 10^{-5} \text{ s}^{-1}$ are found at 6 h just south of the coast (Fig. 5b), which is comparable to seasonal values in Fig. 4b. The most important diurnal signal is located close to the Guinea Coast represented by a black vertical line around 5° – 6°N , laying over about 1° (around 100 km) on both sides of the coast. This signal is in agreement with the characteristics of a sea breeze/land breeze mechanism as described in previous studies for this region (Gbambie and Steyn 2013; Parker et al. 2017; Coulibaly et al. 2019; Guedje et al. 2019). Indeed, as the SST diurnal cycle is not represented in ERA5, the temperature gradient around Guinea Coast closely follows the diurnal warming and cooling of the land surface (see also Fig. 6):

- at 0 h (Fig. 5a), the land is significantly colder than the sea, which creates an anomalous pressure gradient across the

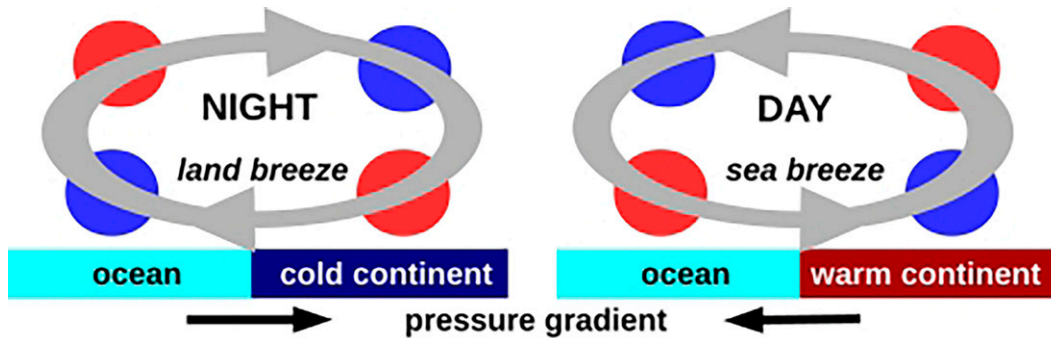


FIG. 6. Scheme of the land–sea breeze during night (cold continent) and day (warm continent). Red disks indicate divergence, and blue ones indicate convergence.

shore and favors a near-surface air circulation from the land toward the sea (Fig. 6, left), superimposed to the strong southerly monsoon flow. A clear meridional surface wind anomaly cannot be seen yet, but the slowing down of southerlies across the coast results in a more convergent surface flow to the south of the coast and divergent to the north (Fig. 6, left). As a result, low-level convection is favored on the ocean side, and rather inhibited on the continent side. The name “land breeze” will thereafter characterize the occurrence of surface wind divergence when it is convergent to the south and divergent to the north of the Guinea Coast.

- at 6 h (Fig. 5b), the land surface temperature is minimal just before sunrise, and the land breeze at its most intense phase: The magnitude of the convergence/divergence dipole is maximal, with a northerly surface wind anomaly and a clear convection/subduction pattern firmly established across the Guinea Coast.
- at 12 h (Fig. 5c), the land has become warmer than the sea, so the land–sea anomalous pressure gradient reverses and strengthens southerlies across the coastline, inducing increased divergence on the sea side which inhibits convection and increased convergence on the land side which strongly favors convection: It will be thereafter called “sea breeze” (Fig. 6, right).
- at 18 h (Fig. 5d), a clear southerly surface wind anomaly across the coast is observed, together with a strong inhibition of convection just south of the coast. In spite of near-surface convergence, the convection is also inhibited on the continent side, suggesting that the sea breeze is going on but may have passed its maximal daily intensity.

To balance the sea breeze/land breeze alternation at the surface, and probably because of mass conservation within the dense monsoon flow (Fig. 6), opposite divergent/convergent dipoles overhanging the surface ones appear between 950 and 800 hPa, especially on the land side. Their change of sign is clearly visible between 6 and 12 h (Figs. 5b,c).

Surface parameters with an hourly resolution make possible an in-depth investigation of the diurnal cycle in ERA5. SKT diurnal cycle shows a constant surface temperature of about 28°C over the ocean, while it varies over the continent

between 24°C in the night and 31°C in the day (Fig. 7b, black contours). A comparison between the surface temperature gradient (thereafter $dSKT/dY$, Fig. 7b, shading) and the 10-m wind divergence (Fig. 7c, shading) confirms that these two parameters undergo strong in-phase diurnal cycles. The “land breeze” phase is longer (around 14 h) than the “sea breeze” phase (around 8 h): The land breeze (negative $dSKT/dY$ in Fig. 7b, and convergence south/divergence north of the coastline in Fig. 7c) starts after 18 h in the early night and does not end before 8–9 h in the following morning, with a seemingly maximum intensity around 6 h just before sunrise. The sea breeze (positive $dSKT/dY$ in Fig. 7b, and divergence south/convergence north of the coastline in Fig. 7c) occurs during the rest of the day, i.e., between 10 and 18 h, with a time lag of about 2 h between the warmest value of $dSKT/dY$ (around 12–13 h) and the maximum surface wind anomaly (around 14–15 h, Fig. 7c). These results are in agreement with Coulibaly et al. (2019) or Gbambie and Steyn (2013), who documented the diurnal cycle with observations near the coast of Benin (located at 2°E): they similarly found that southerlies are minimum at 6 h and maximum at 15 h in boreal spring and summer. Surface wind therefore closely follows the diurnal pattern of land–sea temperature gradient: just south (north) of the coast, it is briefly divergent (convergent) in the day and longer convergent (divergent) in the night.

A comparison is then made between ERA5 precipitation and surface divergence: Along the Guinea Coast between 5° and 6°N, there is a very good fit between surface wind convergence (Fig. 7c, shading) and precipitation (black contours): precipitation is maximum over the ocean during the night and early morning, when the land breeze convergence also reaches its maximum. Over the continent, precipitation peaks around 14–15 h, at the same time as the sea breeze convergence. Conversely, divergence is associated with little or no precipitation: Over the mainland north of the coast during the night (land breeze, between 18 and 8 h), and in the afternoon over the ocean (sea breeze, 10–18 h). Note that the divergence of the sea breeze also explains the narrow gap of precipitation (about 100 km long) observed just south of the Guinea Coast in early afternoon. Over the ocean south of 5°N, precipitation peaks in ERA5 between 8 and 11 h at 4°N (Fig. 7c). It is very interesting to note that these peaks coincide with a clear

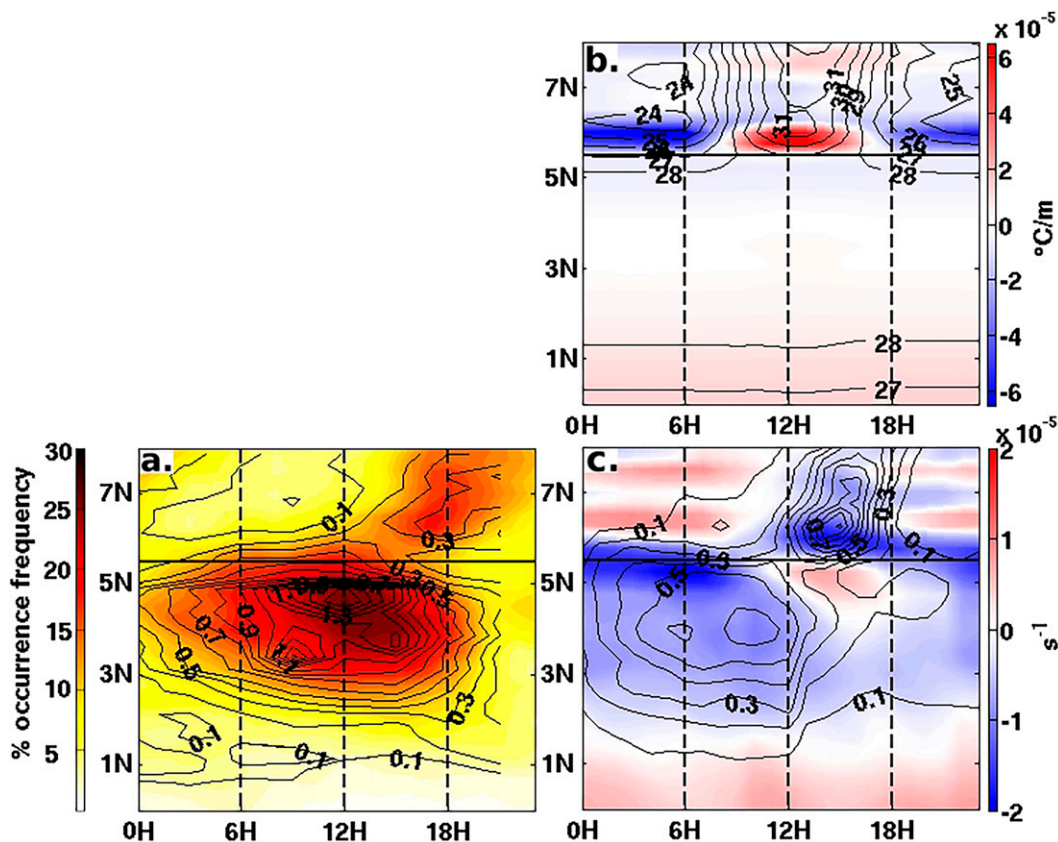


FIG. 7. Time–latitude diurnal composites of 14 days after T_{ref} , $1^{\circ}E-1^{\circ}W$: (a) MSG cloud occurrence (shading; %) and TRMM precipitation (black contours; $mm\ h^{-1}$). (b) ERA5 meridional gradient of SKT (shading; $^{\circ}C\ m^{-1}$) and SKT (black contours; $^{\circ}C$). (c) ERA5 horizontal wind divergence (shading; s^{-1}) and precipitation (black contours; $mm\ h^{-1}$). The black horizontal line stands for the mean coastline latitude.

surface convergence signal that appears to break away from the coast in the early morning. This could be related to an offshore (upstream) propagation of a density front or gravity wave generated at the coast by land breeze convergence, as suggested in studies of tropical coastal regions (Yang and Slingo 2001; Love et al. 2011; Birch et al. 2015; Coppin and Bellon 2019): The overnight and early morning land breeze phase near the coast would then explain why precipitation shows a maximum around noon over the ocean. This signal appears to propagate southward for several hundred kilometers away from the Guinea Coast, at a speed between 10 and $20\ m\ s^{-1}$ (Fig. 7c) with a maximum in the late morning and a minimum in the afternoon/early night, while no significant diurnal cycle can be found in the surface temperature at this location. Similar distances (several hundred km) and propagation speed (about $15\ m\ s^{-1}$) for the daily rainfall maximum were also observed in the observational study of Yang and Slingo (2001) in similar cases. Another hypothesis to explain the diurnal cycle of convection over tropical oceans is that of cloud-radiative effects, e.g., absorption of solar radiation near the cloud top stabilizing the atmosphere during the day, and longwave cooling destabilizing the atmosphere near the cloud top during the night (Wallace 1975), but these

mechanisms account for a convection peak during the night and not in the late morning as here.

On the continent, between 10 and 18 h, a convergence signal appears to extend northward for 100–200 km from the coast (Fig. 7c). It probably favors deep atmospheric convection, with a precipitation anomaly peaking around 14–15 h, as noted in previous studies (Parker et al. 2017). Development of mesoscale convective systems and precipitation in southern West Africa is often associated with wave disturbances, or African easterly waves, which modulate deep convection and rainfall on daily time scales (Fink and Reiner 2003): They explain between 30% and 40% of the convection variance in boreal summer (Mekonnen et al. 2006) and are the main contributor to the West African monsoon precipitation in summer. The low-level convergence in the afternoon associated with the sea breeze would then favor the peak of precipitation observed around 15 h over the continent during the passage of such a disturbance.

These analyses were repeated with observed precipitation (TRMM) and convective cloud occurrence (MSG). They show convective peaks similar to those found in ERA5: Over the ocean in the middle of the day, and over the continent in the afternoon (Fig. 7a). However, as already seen in the

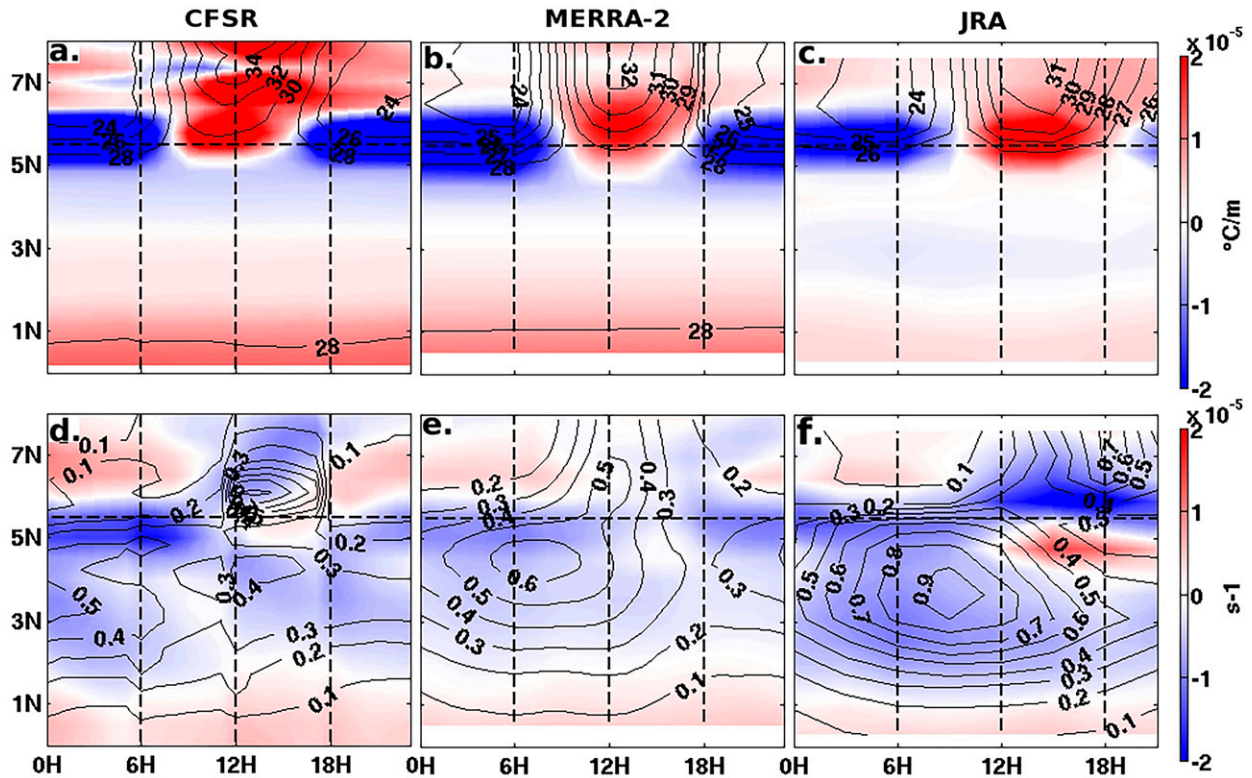


FIG. 8. Time–latitude diurnal composites of 14 days after T_{ref} , 1°E – 1°W , in (left) CFSR, (center) MERRA2, and (right) JRA. (top) Meridional gradient of SKT (shading; K m^{-1}) and SKT (black contours; K). (bottom) Surface wind divergence (shading; s^{-1}) and precipitation (black contours; mm h^{-1}). The black dashed line stands for the mean coastline latitude.

meridional profiles shown in Fig. 4b, the precipitation in ERA5 is about half as large as in the observations. Moreover, the precipitation peaks occur about 3 h too early in ERA5: around 13–15 h instead of 18 h over the continent, and around 8–11 h instead of 12 h over the ocean. This flaw, which is found in most global climate and numerical weather prediction models, could be due to insufficient horizontal grid resolutions or wrong representation of vertical atmospheric stability (Guichard et al. 2004).

The previous results show that on the diurnal scale, the surface temperature gradient controls the surface wind divergence, which in turn controls precipitation. This hypothesis was tested by a similar analysis performed with three other reanalysis sets: CFSR, MERRA-2, and JRA (Fig. 8). Probably because of their coarser horizontal resolutions, the diurnal anomalies of the coastal $d\text{SKT}/dY$ extend somewhat farther from the Guinea Coast, but CFSR (Fig. 8a) and MERRA2 (Fig. 8b) show sign changes at 0800–0900 and 1600–1700 UTC, as in ERA5. In JRA (Fig. 8c), the changes occur instead at 10–11 and 18–19 h, probably due to a different parameterization of the land surface pattern. However, all three surface wind divergence models show a clear overnight and morning land breeze signal near the coast, with a precipitation maximum that appears to “break away” from the most intense convergent signal (Figs. 8d–f). In CFSR, the oceanic precipitation peak is much too low (0.4 mm h^{-1}) but at about the right time

(12–18 h) and at the right latitude (4°N), despite visible discontinuities in the data every 6 h due to forecasts reset. In MERRA2, the peak is just over 0.6 mm h^{-1} at 4° – 5°N , but much too early in the day (6–8 h). And in JRA, it is almost 1 mm h^{-1} , but a little too far south (3° – 4°N) and too early (8–10 h) compared to observations. There is no sea breeze in MERRA2, but a brief neutralization of the land breeze between 12 and 18 h, a relatively weak sea breeze in CFSR also between 12 and 18 h, and a very strong one in JRA between 12 and 0 h. The best representation of continental precipitation is in JRA, with a peak of precipitation around 18 h, as in the observations, which is probably explained by the “sea breeze” that occurs later in the day than in the other reanalyses. However, the representation of diurnal oceanic precipitation in JRA is not better than in ERA5 compared to the observations. This is confirmed in the next section when we examine the diurnal cycle after the end of GCR. This comparison shows a robust impact of the surface temperature gradient on precipitation, and justifies the use of ERA5 as the best compromise to study the processes involved in the control of precipitation by surface temperature.

In summary, the diurnal cycle of $d\text{SKT}/dY$ over the Guinea Coast explains the diurnal cycle of surface wind divergence and precipitation in ERA5 very well, and shares the main characteristics of precipitation and convective clouds found in the observations (Fig. 7). In particular, an onshore breeze-like

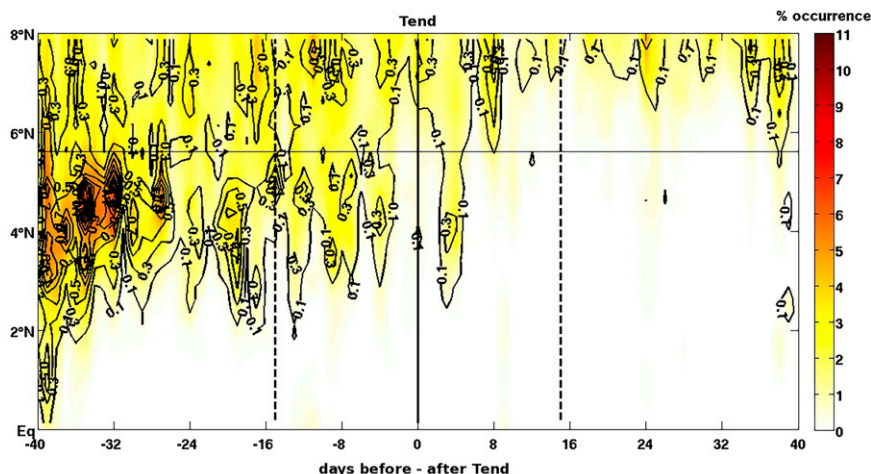


FIG. 9. Time–latitude seasonal composites around T_{end} , 1°W – 1°E , of convective clouds frequency (shading; %) and TRMM precipitation (black contours; intervals of 0.2 mm h^{-1} starting at 0.1 mm h^{-1}). The vertical black line stands for lag 0 (T_{end}), dashed ones represent ± 15 days. The black horizontal line stands for the mean coastline latitude.

signal appears to favor significant precipitation over the ocean with an early morning peak, and a sea breeze–like signal appears to be related to a late afternoon peak in precipitation over the continent. The duration of the onshore breeze is on average much longer during the day than that of the offshore breeze, which may partly explain why GCR precipitation is more abundant over the ocean than over the continent (Fig. 1b). The emergence of the coastal upwelling in July should then reduce the nighttime land–sea temperature difference, and hence the intensity of the onshore breeze phase, and control the disappearance of coastal precipitation. This hypothesis is examined in the next section using composites built around an estimate of the date of the GCR demise.

5. Demise of the Guinea Coast rainfall

An estimation of the date of the GCR demise was not possible using the satellite surface wind as for T_{ref} , since the satellite cannot properly provide wind data within 50 km of the coast. Moreover, the transition from the GCR to the Little Dry Season is not as clear-cut as the cessation of precipitation south of 3°N at T_{ref} as discussed in section 2. Instead, a GCR demise date, T_{end} , is computed based on the observed (Reynolds product) SST: A zone is defined between 2.5°W and 3°E , 1° – 2.5° south of the coast, and an SST index is averaged in this zone from April to July 2008–15. An additional index (of the SST gradient) is also computed by subtracting the SST at the northern edge of this area from the SST at the southern edge, in order to better characterize the seasonal cooling in the coastal upwelling in late June–July, independently of the strong SST interannual variability. The T_{end} is then chosen as the first day when the two following criteria are true until the end of July:

- the SST index must be lower than 80% of its values, and
- the magnitude of the SST gradient index must be larger than 20% of the total magnitudes.

This definition is not very precise and the date typically varies by a few days by slightly modifying the two criteria defined just above; however, it allows us to characterize the emergence of the coastal upwelling with sufficient accuracy, despite its large interannual variability: The average T_{end} between 2008 and 2015 is 14 July, with values ranging from 28 June to 31 July. Note that T_{end} is different from the “monsoon jump” date discussed in many previous studies [see e.g., Fitzpatrick et al. (2015)]: The latter defines the date when the zonal band of precipitation, often averaged between 10°W and 10°E , makes a sudden northward excursion and reaches the latitude of the Sahel (Sultan and Janicot 2003), whereas the definition of T_{end} here is intended to target the onset of the Little Dry Season for the Guinea Coast countries, and these two events are apparently unrelated (see Fig. A2).

A daily time/latitude composite built around T_{end} and averaged between 1°W and 1°E documents the precipitation and convective clouds during 80 days before and after T_{end} (Fig. 9). A rather noisy variability remains visible at the daily time scale, but a clear seasonal trend can be noticed: The TRMM precipitation and MSG convective cloud composites show that T_{end} corresponds very well to the transition between the GCR and the little dry season, with abundant precipitation and convective clouds between 3° and 6°N before T_{end} (at negative lags) and very scarce after T_{end} (positive lags); only a brief precipitation event (a little more than 0.1 mm h^{-1}) is observed 3–4 days after T_{end} . The Little Dry Season is then clearly visible in this composite, with an almost complete absence of precipitation (less than 0.1 mm h^{-1}) and very few convective clouds from 8 days after T_{end} until 30 days later (Fig. 9), which is consistent with the hypothesis that the emergence of the coastal upwelling partly controls the end of the GCR around mid-July on average. The involved mechanisms are then investigated in ERA5 reanalyses.

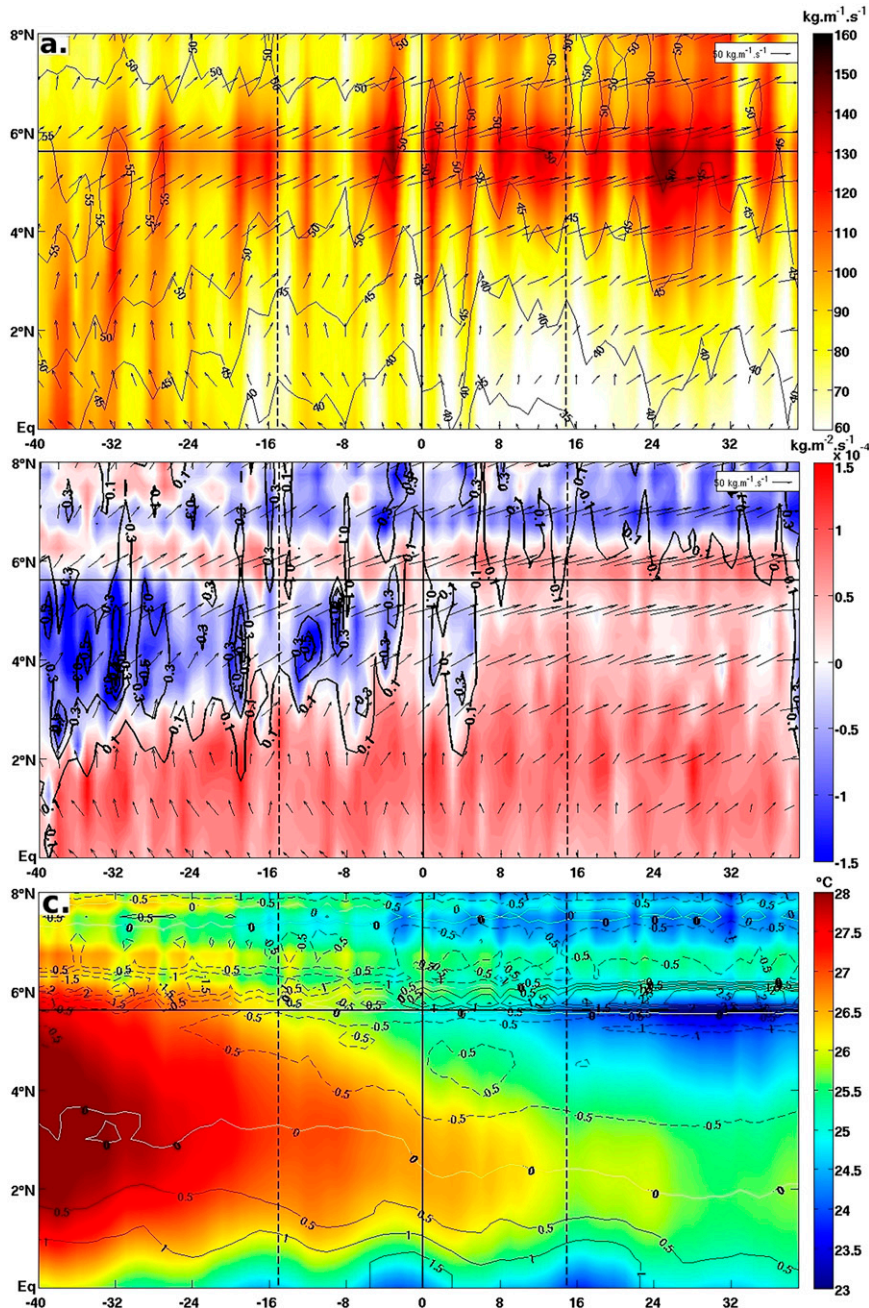


FIG. 10. Time-latitude seasonal composites around T_{end} , 1°W-1°E, in ERA5 reanalyses. (a) Module (shading; $\text{kg}\cdot\text{m}^{-1}\cdot\text{s}^{-1}$) and direction (arrows) of the humidity transport integrated between 1000 and 850 hPa and total column water vapor (black contours; intervals of $5\text{ kg}\cdot\text{m}^{-2}$). (b) Humidity transport [represented by similar arrows as in (a)], divergence (shading; $\text{kg}\cdot\text{m}^{-2}\cdot\text{s}^{-1}$), and ERA5 precipitation (black contours; intervals of $0.2\text{ mm}\cdot\text{h}^{-1}$, starting at $0.1\text{ mm}\cdot\text{h}^{-1}$). (c) SKT (shading; $^{\circ}\text{C}$) and meridional gradient of SKT (black contours, intervals of $0.5 \times 10^{-5}\text{ }^{\circ}\text{C}\cdot\text{m}^{-1}$; white contours indicate null gradient).

Although precipitation in ERA5 are about half that in the observations particularly during intense rainfall events (the contours of precipitation peaks show several maximums around $0.5\text{ mm}\cdot\text{h}^{-1}$ in Fig. 10b, against over $1\text{ mm}\cdot\text{h}^{-1}$ in Fig. 9),

its composite shows a very good match with the observations, showing a similar abrupt transition between abundant precipitation south of the Guinea Coast before T_{end} and very sparse precipitation thereafter (Fig. 10b, black contours).

Since humidity is mainly confined in the monsoon flow in the region of scrutiny, the humidity transport was integrated between 1000 and 850 hPa and its seasonal composite computed around T_{end} . South of 3°N , the northward moisture transport is quite large before T_{end} , and decreases sharply after T_{end} (Fig. 10a, shading), turning west/southwest. In the coastal region between $3^{\circ}\text{--}4^{\circ}\text{N}$ and 6°N , it rather increases after T_{end} and clearly turns more and more eastward throughout the season. The same is true for the humidity transport north of 6°N , except that it increases more strongly from before to after T_{end} . This is consistent with previous studies that report a significant input of humidity into West Africa summer monsoon from the eastern Atlantic, via the low-level West African westerly jet (Pu and Cook 2012). It becomes on average larger than the humidity transport from the south after the monsoon jump in summer (Lélé et al. 2015).

In agreement with the low-level humidity transport, the total column water vapor (TCWV) exhibits a maximum just south of the Guinea Coast before T_{end} , then this maximum slowly migrates farther north (Fig. 10a, black contours). This migration follows the African easterly jet (AEJ) localized around 600–700 hPa (not shown), north of the TCWV maximum, its latitude is controlled by the land surface temperature and soil moisture distribution (Cook 1999): Its presence induces strong vertical wind shear and horizontal vorticity, which, combined with the high TCWV value, lead to the formation of mesoscale convective systems that contribute largely to the GCR. However, the northward progression of the TCWV (Fig. 10a, black contours) is visibly smoother than the abrupt shift observed in precipitation (Fig. 10b, black contours). A much better match is found between precipitation and the divergence of low-level humidity transport (Fig. 10b, shading), which is minimum and negative (i.e., convergent) where precipitation is the largest. The seasonal evolution of the humidity transport convergence can then be explained by that of the ocean surface temperature, as sketched in Fig. 2. Between T_{ref} and T_{end} , the low-level humidity transport is divergent south of 3°N and convergent between 3°N and the Guinea Coast (Fig. 10b, negative lags), forced by the emergence of the northern front of the oceanic cold tongue observed around $1^{\circ}\text{--}2^{\circ}\text{N}$ (Fig. 10c). As the coastal upwelling emerges, after T_{end} , a negative $d\text{SKT}/dY$ signal develops rapidly just south of the Guinea Coast with a peak shortly after T_{end} (Fig. 10c, black contours): we suggest that this peak contributes to dampening the convergence of humidity transport against the coast by slowing down the low-level southerlies, which would favor less oceanic precipitation near the coast (see also Fig. 2). Note that both mechanisms are probably involved here, the negative $d\text{SKT}/dY$ forcing a positive meridional pressure gradient, as well as the SST cooling increasing vertical stability in the core of the coastal upwelling. As a result, the negative $d\text{SKT}/dY$ signal just after T_{end} clearly corresponds to a concomitant demise of coastal oceanic precipitation.

Examination of the diurnal cycle provides a better understanding of this oceanic control over precipitation: In the coastal region ($4^{\circ}\text{--}7^{\circ}\text{N}$), before T_{end} , low-level humidity

transport is strongly convergent over the ocean and slightly divergent over the continent (Fig. 10b, negative lags until -2 days), consistent with a land breeze that would be of greater amplitude than the sea breeze on a daily average. After T_{end} , the decrease in humidity transport convergence over the ocean at daily time scale can then be explained by a weaker land breeze phase. It is indeed what is observed in the diurnal after- T_{end} composite (Fig. 11c) compared to the after T_{ref} composite (Fig. 7c): absolute values of low-level convergence just south of the coast in the night and morning drop from about $2 \times 10^{-5} \text{ s}^{-1}$ after T_{ref} to about $1 \times 10^{-5} \text{ s}^{-1}$ after T_{end} . And this weakening of the land breeze can be explained by the decrease in the land–sea temperature difference during the night, following the emergence of the coastal upwelling (Fig. 11b, compared to Fig. 7b).

However, ERA5 precipitation tends to slightly persist after T_{end} over the ocean, as it can be observed in its diurnal cycle averaged on the 15 days after T_{end} . Values larger than 0.1 mm h^{-1} are mostly found in the morning (Fig. 11c), while morning precipitation hardly reaches this value in the observations (Fig. 11a). In addition, too much continental precipitation, in phase with a peak of sea-breeze surface convergence just north of the coast, occurs in ERA5 in the afternoon (Fig. 11c), whereas a rather modest convective activity is seen in the observations (Fig. 11a). And no continental precipitation is found in ERA5 during the night and early morning, probably in response to the land-breeze divergence signal between 21 and 9 h (Fig. 11c), whereas a weak but continuous convective activity can be tracked in the observations (Fig. 11a). This suggests that, although the GCR seasonal evolution is much better represented in ERA5 reanalyses than in previous reanalyses, its diurnal cycle is strongly controlled by the land–sea breeze near the coast in ERA5, even after T_{end} when this seems to be no longer the case in the observations. Despite these shortcomings, the results of this section clearly indicate that, by decreasing the northward transport of humidity south of the Guinea Coast and its convergence against the coast, the emergence of the coastal upwelling may well contribute to the end of the GCR and the beginning of the Little Dry Season. In addition, this would also explain why the supply of humidity from the southern monsoon flow decreases in favor of that from the eastern Atlantic via the low-level African westerly jet over the continent at about this time.

6. Summary and conclusions

The present study focuses on the northern Gulf of Guinea, between Benin and Ivory Coast, where observed SST data between 2008 and 2015 were used to estimate the onset (T_{ref}) and demise (T_{end}) dates of the Guinea Coast rainfall (GCR), i.e., the coastal stage of the West African monsoon, in June on average, before it reaches the Sahel in summer. Composites of ERA5 reanalyses and observations of precipitation and convective cloud cover are shown. The issue is to investigate whether the diurnal and seasonal composites of surface temperature and oceanic or near-coastal continental

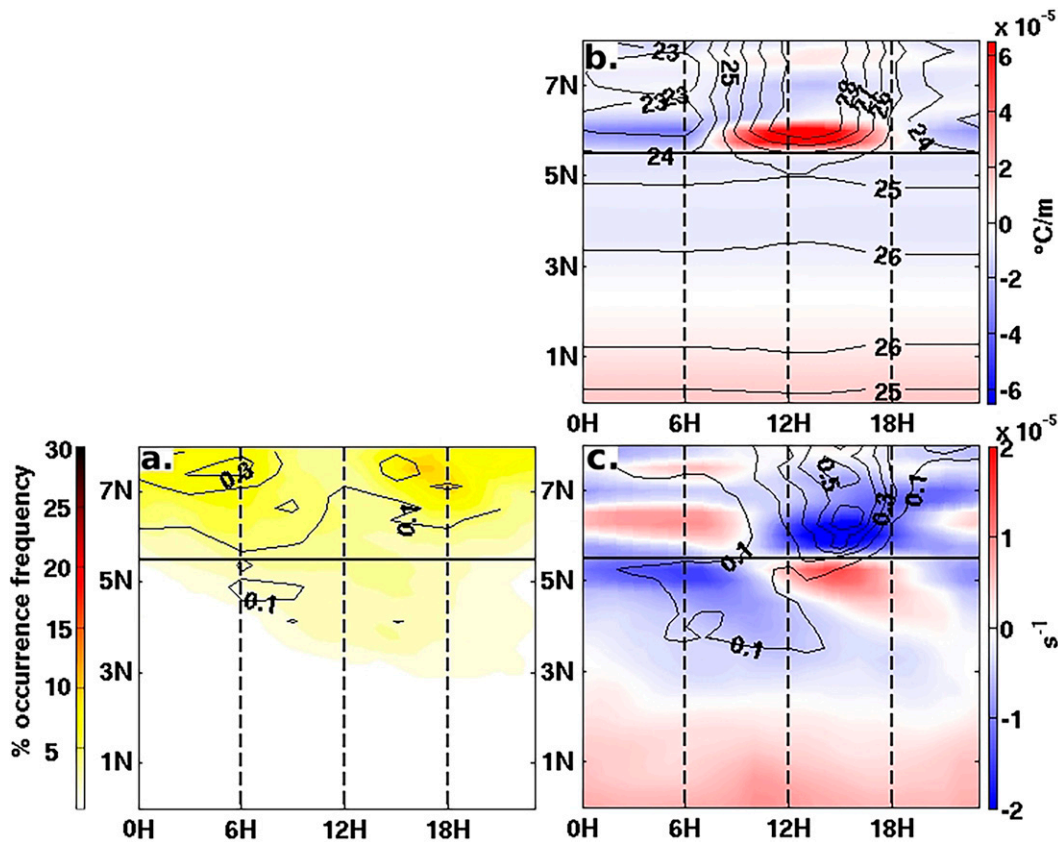


FIG. 11. As in Fig. 7, but for the time–latitude diurnal composites of 14 days after T_{end} instead of T_{ref} .

low-level circulation could help to understand the conditions of GCR onset and demise dates.

The onset date T_{ref} was obtained by using a criteria based on low-level atmospheric dynamics, which is related to the SST cooling in the equatorial upwelling region (also known as the Atlantic cold tongue). The near-equatorial SST front strengthens the surface wind to the north and weakens it to the south, as sketched in Fig. 2 (middle): The low-level humidity transport becomes strongly divergent south of 3°N , which inhibits deep atmospheric convection and precipitation, and convergent between 3°N and the Guinea Coast, explaining the GCR onset.

This was already known from previous studies (Meynadier et al. 2015; Leduc-Leballeur et al. 2013), but in addition, the diurnal cycle computed with the hourly ERA5 data helped to explain why the GCR precipitation mainly occurs over the ocean: oceanic precipitation starts after sunset until about noon in the following day, in ERA5 as well as in observations, in very good agreement with the diurnal cycle of surface wind convergence found in ERA5 just south of the coast. The latter is in phase with the inversion of $d\text{SKT}/dY$ across the coast, which forces a land breeze from about 19 h until 11 h the next day. In addition, a signal seems to detach southward from the coast in late night/early morning: It could correspond to a gravity wave emitted as the land breeze is about to give way

to the sea breeze, and explain why a maximum is found in ERA5 precipitation as far as 400–500 km from the coast during the morning/early afternoon (from noon to late afternoon in the observations). Similar results were found with three other reanalysis ensembles, although their representation of the diurnal cycle is not as good as in ERA5. Despite an early shift of the diurnal cycle, probably due to problems in modeling surface temperature cycle, this confirms that the diurnal cycle of the coastal $d\text{SKT}/dY$ does drive the diurnal cycle of the surface wind convergence near the coast.

As suggested by previous studies, the coastal upwelling that emerges in July along the Guinea Coast has a strong impact on the disappearance of the GCR and the onset of the Little Dry Season. SST and SST gradient indices in the core of the coastal upwelling, calculated from observations, were used to estimate a date of emergence of the coastal upwelling, T_{end} : With an accuracy of a few days, this date is preceded by a slow decrease of the GCR, and coincides with its rather abrupt disappearance, both in ERA5 and observations. In ERA5, the decrease in oceanic precipitation is clearly explained by the decrease in convergence of the low-level humidity transport just south of the Guinea coast, which slowly decreases before T_{end} and disappears soon after. Just south of the coast, a strong meridional–negative–SST gradient is found when the upwelling emerges: By decreasing the southerlies

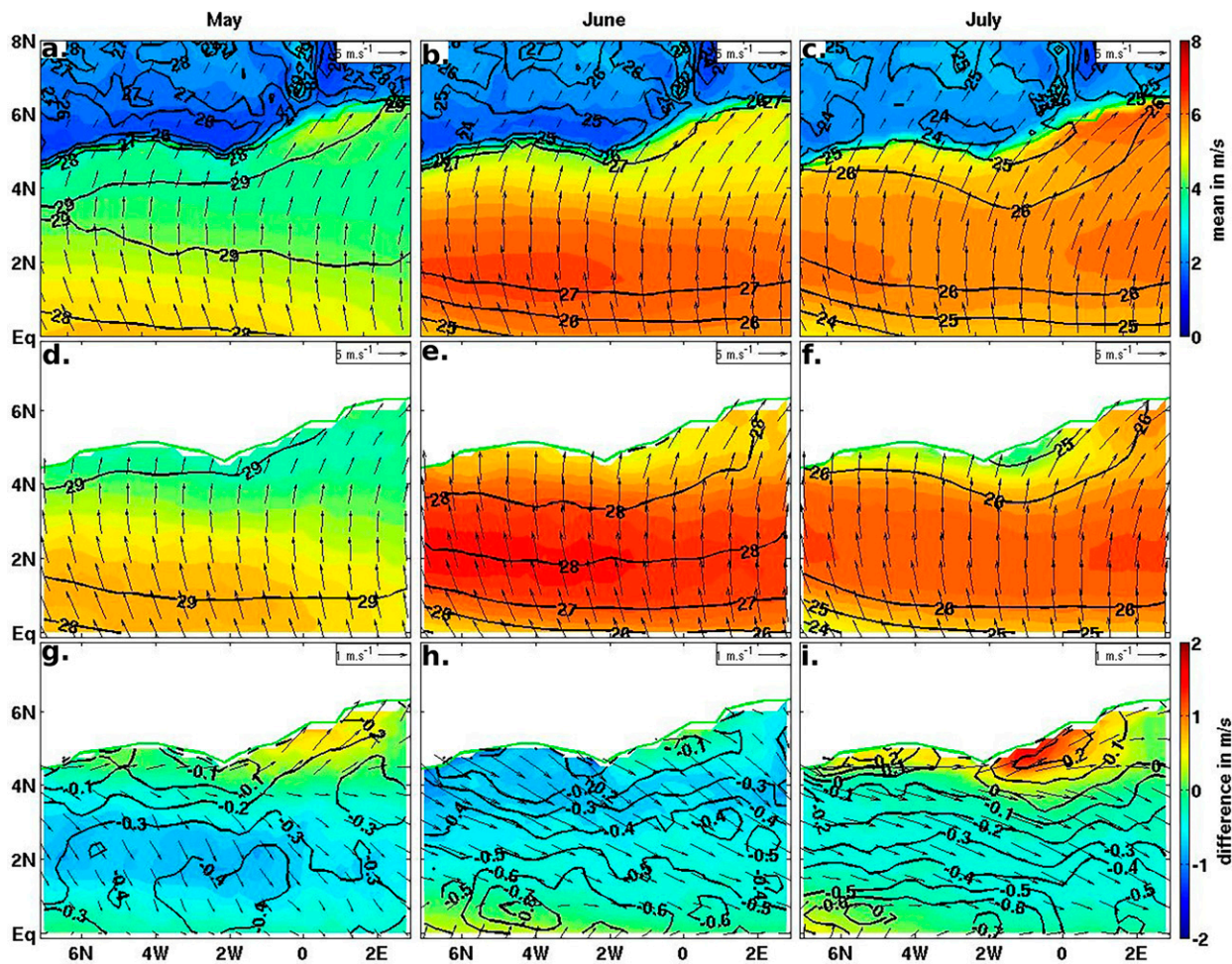


FIG. A1. 2008–15 climatology in (left) May, (center) June, and (right) July of surface wind speed (black arrows; magnitude in shading; $m s^{-1}$) and SKT (black contours; intervals of $1^{\circ}C$) in (a)–(c) ERA5, (d)–(f) observations (wind ASCAT and SST Reynolds), and (g)–(i) their difference.

near the coast, it counteracts the effect of the positive SST gradient north of the cold tongue front which intensifies them. This can clearly explain the decrease in near-coastal convergence of low-level humidity and precipitation (Fig. 2, bottom). Moreover, on the diurnal scale, a weaker land breeze after T_{end} , due to a lower land–sea temperature difference during the night because of the emergence of the coastal upwelling, also contributes to the decrease in near-coastal convergence and the GCR demise.

These assumptions are based on seasonal composites calculated over only eight years, and obviously require further investigation. If the impact of coastal upwelling on the disappearance of the GCR in July were to be confirmed, it would be of major importance to determine more precisely the mechanisms of this impact, and to verify that it is well represented in the weather forecasting models. Indeed, the large-scale surface wind probably controls a large part of the fluctuations of the coastal upwelling on synoptic and intraseasonal scales: A feedback of this upwelling on the regional atmospheric circulation could have a great importance

on the seasonal evolution of precipitation, its intraseasonal variability, and its seasonal predictability. A poor representation of this feedback could, for example, partly explain why the end of coastal precipitation is generally poorly represented in climate models.

One element that may be important in this feedback and has not been discussed here is the low-level cloud cover: It is a key element controlling the land–sea breeze in the surface energy balance, and has been investigated in several studies (Knippertz et al. 2011). The intensive measurement campaign of the European project Dynamics–Aerosol–Chemistry–Cloud Interactions in West Africa (DACCIWA) in June–July 2016 provided important in situ data documenting the land–sea breeze in Ghana, Togo, and Benin, and the interaction between low-level clouds and the emission of aerosol pollutants by megacities such as Lome or Lagos in Nigeria (Knippertz et al. 2017). These data could help to perform a full validation and estimation of the ERA5 reanalyses. We therefore intend to extend the present study to the representation of the processes involved in coastal precipitation

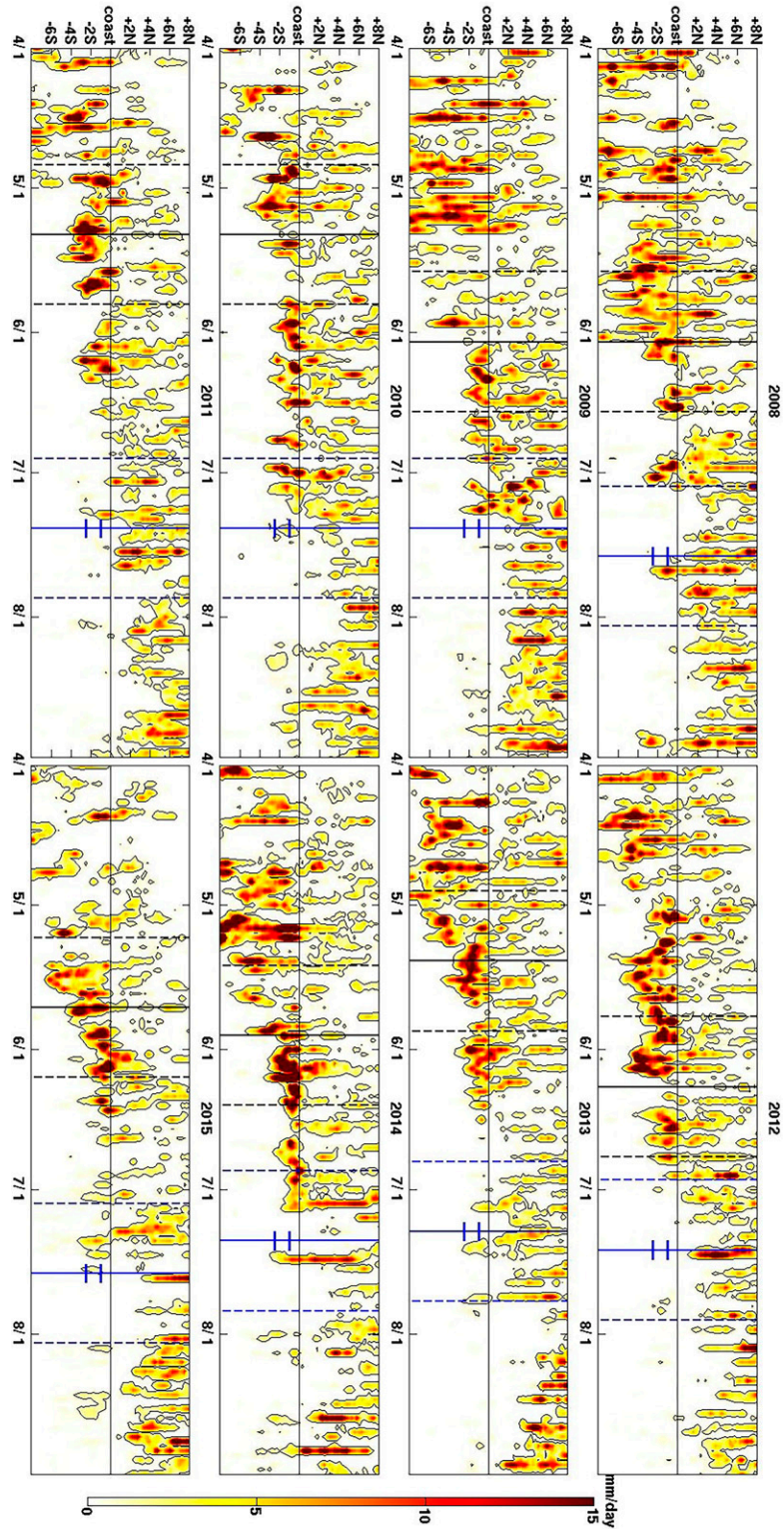


FIG. A2. Precipitation 1°W–1°E for all specific years between 2008 and 2015.

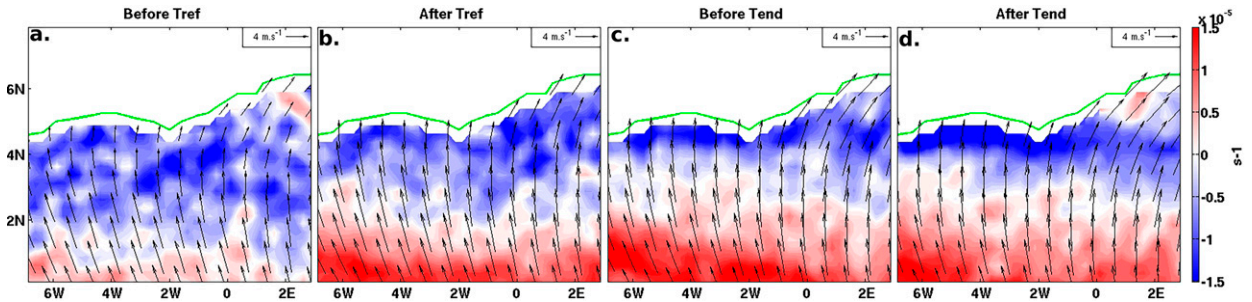


FIG. A3. As in Figs. 3a and 3b, but for ASCAT surface wind and divergence, and (c) before and (d) after T_{end} as well as (a) before and (b) after T_{ref} .

at intraseasonal time scales in ERA5 reanalyses. In addition, numerical simulations, for example with a regional atmospheric model forced by coastal upwellings of varying intensities, should also allow us to estimate the importance of coastal upwelling by isolating its impact. Finally, a similar study is needed for the second coastal precipitation season: The southward migration of precipitation to the ocean in September–November is much smoother than the northward migration in summer studied in this paper, which could also help to better understand the mechanisms involved here.

Acknowledgments. We thank the anonymous reviewers for their comments, which were of great help in improving

the manuscript, and Geneviève Seze in her help using the SEVIRI cloud products. Funding: Manuel Tanguy has a Ph.D. fellowship from UVSQ.

Data availability statement. This study benefits from SEVIRI cloud products produced and distributed by AERIS/ICARE Data and Services Center, and for which we would like to thank Geneviève SEZE; ERA-5 reanalyses are from Copernicus Climate Change Service, available from the IPSL/ESPRI mesocenter. We also thank the NOAA/NCDC for Reynolds SST product and NOAA for ASCAT wind product used, and the Institut Pierre-Simon Laplace and LATMOS for server and data storage (Climserv and Ciclad). Availability of data

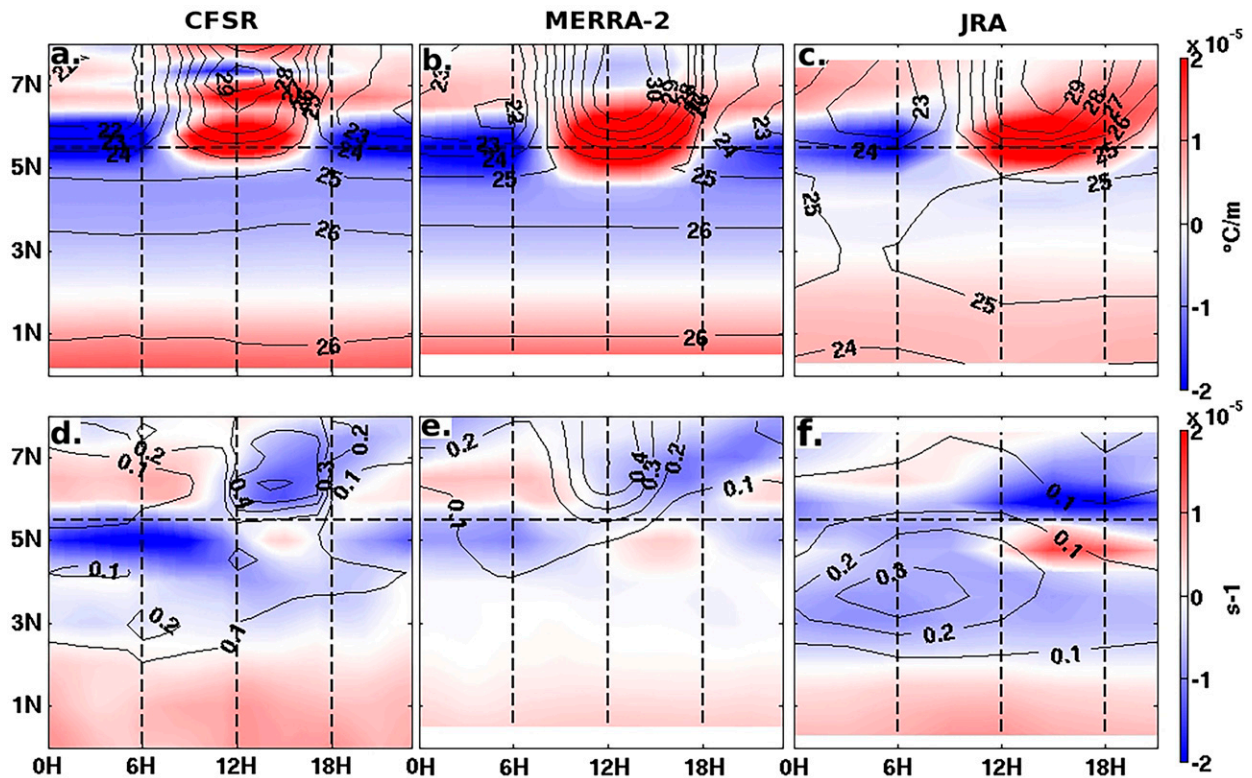


FIG. A4. As in Fig. 8, but after T_{end} .

and material (data transparency). All sources of data have been mentioned and are in free access. Code availability (software application or custom code): yes, on demand. Conflicts of interest/competing interests (include appropriate disclosures): none.

APPENDIX A

Additional Figures

Figure A1 compares the monthly means of wind and skin temperature in May–July between reanalysis and observation-based datasets. **Figures A2** and **A3**, respectively, detail the seasonal evolution of precipitation and wind based on observational datasets. **Figure A4** shows the diurnal composites of temperature convergence and precipitation after the coastal upwelling formation in CFSR MERRA2 and JRA datasets, illustrating our discussion with less reliance of a particular modelization.

REFERENCES

- Abayomi, A. A., B. J. Abiodun, and B. J. Omotosho, 2007: An observational study of sea breeze over Nigerian coastal region. *Res. J. Appl. Sci.*, **2**, 745–751.
- Adejuwon, J. O., and T. O. Odekunle, 2006: Variability and the severity of the “Little Dry Season” in southwestern Nigeria. *J. Climate*, **19**, 483–493, <https://doi.org/10.1175/JCLI3642.1>.
- Akinsanola, A. A., K. O. Ogunjobi, V. O. Ajayi, E. A. Adefisan, J. A. Omotosho, and S. Sanogo, 2017: Comparison of five gridded precipitation products at climatological scales over West Africa. *Meteor. Atmos. Phys.*, **129**, 669–689, <https://doi.org/10.1007/s00703-016-0493-6>.
- Ali, K. E., K. Y. Kouadio, E.-P. Zahiri, A. Aman, A. P. Assamoi, and B. Bourles, 2011: Influence of the Gulf of Guinea coastal and equatorial upwellings on the precipitations along its northern coasts during the boreal summer period. *Asian J. Appl. Sci.*, **4**, 271–285, <https://doi.org/10.3923/ajaps.2011.271.285>.
- Aman, A., E. Toualy, and F. Yoroba, 2018: On the causes of the minor dry season over the coastal region of the northern Gulf of Guinea. *Atmos. Climate Sci.*, **8**, 121–133, <https://doi.org/10.4236/acs.2018.82009>.
- Bakun, A., 1978: Guinea current upwelling. *Nature*, **271**, 147–150, <https://doi.org/10.1038/271147a0>.
- Bechtold, P., N. Semane, P. Lopez, J.-P. Chaboureaud, A. Beljaars, and N. Bormann, 2014: Representing equilibrium and nonequilibrium convection in large-scale models. *J. Atmos. Sci.*, **71**, 734–753, <https://doi.org/10.1175/JAS-D-13-0163.1>.
- Birch, C. E., M. J. Roberts, L. Garcia-Carreras, D. Ackerley, M. J. Reeder, A. P. Lock, and R. Schiemann, 2015: Sea-breeze dynamics and convection initiation: The influence of convective parameterization in weather and climate model biases. *J. Climate*, **28**, 8093–8108, <https://doi.org/10.1175/JCLI-D-14-00850.1>.
- Bony, S., and Coauthors, 2015: Clouds, circulation and climate sensitivity. *Nat. Geosci.*, **8**, 261–268, <https://doi.org/10.1038/ngeo2398>.
- Caniaux, G., H. Giordani, J.-L. Redelsperger, F. Guichard, E. Key, and M. Wade, 2011: Coupling between the Atlantic cold tongue and the West African monsoon in boreal spring and summer. *J. Geophys. Res.*, **116**, C04003, <https://doi.org/10.1029/2010JC006570>.
- Chelton, D. B., and Coauthors, 2001: Observations of coupling between surface wind stress and sea surface temperature in the eastern tropical Pacific. *J. Climate*, **14**, 1479–1498, [https://doi.org/10.1175/1520-0442\(2001\)014<1479:OOCBSW>2.0.CO;2](https://doi.org/10.1175/1520-0442(2001)014<1479:OOCBSW>2.0.CO;2).
- , M. G. Schlax, M. H. Freilich, and R. F. Milliff, 2004: Satellite measurements reveal persistent small-scale features in ocean winds. *Science*, **303**, 978–983, <https://doi.org/10.1126/science.1091901>.
- Cook, K. H., 1999: Generation of the African easterly jet and its role in determining West African precipitation. *J. Climate*, **12**, 1165–1184, [https://doi.org/10.1175/1520-0442\(1999\)012<1165:GOTAEJ>2.0.CO;2](https://doi.org/10.1175/1520-0442(1999)012<1165:GOTAEJ>2.0.CO;2).
- Copernicus Climate Change Service, 2017: ERA5: Fifth generation of ECMWF atmospheric reanalyses of the global climate. C3S, accessed 18 April 2019, <https://www.ecmwf.int/en/forecasts/dataset/ecmwf-reanalysis-v5>.
- Coppin, D., and G. Bellon, 2019: Physical mechanisms controlling the offshore propagation of convection in the tropics: 2. Influence of topography. *J. Adv. Model. Earth Syst.*, **11**, 3251–3264, <https://doi.org/10.1029/2019MS001794>.
- Coulibaly, A., B. J. Omotosho, M. B. Sylla, A. Coulibaly and A. Ballo, 2019: Characteristics of land and sea breezes along the Guinea Coast of West Africa. *Theor. Appl. Climatol.*, **138**, 953–971, <https://doi.org/10.1007/s00704-019-02882-0>.
- Crespo, L. R., N. Keenlyside, and S. Koseki, 2019: The role of sea surface temperature in the atmospheric seasonal cycle of the equatorial Atlantic. *Climate Dyn.*, **52**, 5927–5946, <https://doi.org/10.1007/s00382-018-4489-4>.
- Derrien, M., and H. L. Gléau, 2005: MSG/SEVIRI cloud mask and type from SAFNWC. *Int. J. Remote Sens.*, **26**, 4707–4732, <https://doi.org/10.1080/01431160500166128>.
- , and —, 2010: Improvement of cloud detection near sunrise and sunset by temporal-differencing and region-growing techniques with real-time SEVIRI. *Int. J. Remote Sens.*, **31**, 1765–1780, <https://doi.org/10.1080/01431160902926632>.
- Djakouré, S., P. Penven, B. Bourlès, V. Koné, and J. Veitch, 2017: Respective roles of the Guinea Current and local winds on the coastal upwelling in the northern Gulf of Guinea. *J. Phys. Oceanogr.*, **47**, 1367–1387, <https://doi.org/10.1175/JPO-D-16-0126.1>.
- Fink, A. H., and A. Reiner, 2003: Spatiotemporal variability of the relation between African easterly waves and West African squall lines in 1998 and 1999. *J. Geophys. Res.*, **108**, 4332, <https://doi.org/10.1029/2002JD002816>.
- , and Coauthors, 2017: Mean climate and seasonal cycle. *Meteorology of Tropical West Africa*, D. J. Parker and M. Diop-Kane, Eds., John Wiley and Sons, 1–39, <https://doi.org/10.1002/9781118391297.ch1>.
- Fitzpatrick, R. G. J., C. L. Bain, P. Knippertz, J. H. Marsham, and D. J. Parker, 2015: The West African monsoon onset: A concise comparison of definitions. *J. Climate*, **28**, 8673–8694, <https://doi.org/10.1175/JCLI-D-15-0265.1>.
- Flamant, C., and Coauthors, 2018: Aerosol distribution in the northern Gulf of Guinea: Local anthropogenic sources, long-range transport, and the role of coastal shallow circulations. *Atmos. Chem. Phys.*, **18**, 123 63–123 89, <https://doi.org/10.5194/acp-18-12363-2018>.
- Gbambie, A. S. B., and D. G. Steyn, 2013: Sea breezes at Cotonou and their interaction with the West African monsoon. *Int. J. Climatol.*, **33**, 2889–2899, <https://doi.org/10.1002/joc.3637>.
- Gelaro, R., and Coauthors, 2017: The Modern-Era Retrospective Analysis for Research and Applications, version 2 (MERRA-2).

- J. Climate*, **30**, 5419–5454, <https://doi.org/10.1175/JCLI-D-16-0758.1>.
- Giannini, A., R. Saravanan, and P. Chang, 2003: Oceanic forcing of Sahel rainfall on interannual to interdecadal time scales. *Science*, **302**, 1027–1030, <https://doi.org/10.1126/science.1089357>.
- Gleixner, S., T. Demissie, and G. T. Diro, 2020: Did ERA5 improve temperature and precipitation reanalysis over East Africa? *Atmosphere*, **11**, 996, <https://doi.org/10.3390/atmos11090996>.
- Gu, G., and R. F. Adler, 2004: Seasonal evolution and variability associated with the West African monsoon system. *J. Climate*, **17**, 3364–3377, [https://doi.org/10.1175/1520-0442\(2004\)017<3364:SEAVAW>2.0.CO;2](https://doi.org/10.1175/1520-0442(2004)017<3364:SEAVAW>2.0.CO;2).
- Guedje, F. K., A. V. V. Houeto, E. B. Houngrinou, A. H. Fink, and P. Knippertz, 2019: Climatology of coastal wind regimes in Benin. *Meteor. Z.*, **28**, 23–39, <https://doi.org/10.1127/metz/2019/0930>.
- Guichard, F., and Coauthors, 2004: Modelling the diurnal-cycle of deep precipitating convection over land with cloud-resolving models and single-column models. *Quart. J. Roy. Meteor. Soc.*, **130**, 3139–3172, <https://doi.org/10.1256/qj.03.145>.
- Hagos, S. M., and K. H. Cook, 2007: Dynamics of the West African monsoon jump. *J. Climate*, **20**, 5264–5284, <https://doi.org/10.1175/2007JCLI1533.1>.
- Harlaß, J., M. Latif, and W. Park, 2015: Improving climate model simulation of tropical Atlantic sea surface temperature: The importance of enhanced vertical atmosphere model resolution. *Geophys. Res. Lett.*, **42**, 2401–2408, <https://doi.org/10.1002/2015GL063310>.
- Hayes, S. P., M. McPhaden, and J. Wallace, 1989: The influence of sea-surface temperature on surface wind in the eastern equatorial Pacific: Weekly to monthly variability. *J. Climate*, **2**, 1500–1506, [https://doi.org/10.1175/1520-0442\(1989\)002<1500:TIOSST>2.0.CO;2](https://doi.org/10.1175/1520-0442(1989)002<1500:TIOSST>2.0.CO;2).
- Hersbach, H., and Coauthors, 2020: The ERA5 global reanalysis. *Quart. J. Roy. Meteor. Soc.*, **146**, 1999–2049, <https://doi.org/10.1002/qj.3803>.
- Huffman, G. J., and Coauthors, 2007: The TRMM Multisatellite Precipitation Analysis (TMPA): Quasi-global, multiyear, combined-sensor precipitation estimates at fine scales. *J. Hydrometeorol.*, **8**, 38–55, <https://doi.org/10.1175/JHM560.1>.
- IPCC, 2007: *Climate Change 2007: The Physical Science Basis*. Cambridge University Press, 996 pp.
- Johannsen, F., S. Ermida, J. P. A. Martins, I. F. Trigo, M. Nogueira, and E. Dutra, 2019: Cold bias of ERA5 summertime daily maximum land surface temperature over Iberian Peninsula. *Remote Sens.*, **11**, 2570, <https://doi.org/10.3390/rs11212570>.
- Kniffka, A., and Coauthors, 2020: An evaluation of operational and research weather forecasts for southern West Africa using observations from the DACCWA field campaign in June–July 2016. *Quart. J. Roy. Meteor. Soc.*, **146**, 1121–1148, <https://doi.org/10.1002/qj.3729>.
- Knippertz, P., A. H. Fink, R. Schuster, J. Trentmann, J. M. Schrage, and C. Yorke, 2011: Ultra-low clouds over the southern West African monsoon region. *Geophys. Res. Lett.*, **38**, L21808, <https://doi.org/10.1029/2011GL049278>.
- , and Coauthors, 2017: A meteorological and chemical overview of the DACCWA field campaign in West Africa in June–July 2016. *Atmos. Chem. Phys.*, **17**, 10893–10918, <https://doi.org/10.5194/acp-17-10893-2017>.
- Kobayashi, S., and Coauthors, 2015: The JRA-55 reanalysis: General specifications and basic characteristics. *J. Meteor. Soc. Japan*, **93**, 5–48, <https://doi.org/10.2151/jmsj.2015-001>.
- Kouadio, K., S. Bastin, A. Konare, and V. O. Ajayi, 2020: Does convection-permitting simulate better rainfall distribution and extreme over Guinean Coast and surroundings? *Climate Dyn.*, **55**, 153–174, <https://doi.org/10.1007/s00382-018-4308-y>.
- Kouadio, Y. K., S. Djakouré, A. Aman, K. E. Ali, V. Koné, and E. Toualy, 2013: Characterization of the boreal summer upwelling at the northern coast of the Gulf of Guinea based on the PROPAO in situ measurements network and satellite data. *Int. J. Oceanogr.*, **2013**, 816561, <https://doi.org/10.1155/2013/816561>.
- Leduc-Leballeur, M., G. de Coëtlogon, and L. Eymard, 2013: Air–sea interaction in the Gulf of Guinea at intraseasonal time-scales: Wind bursts and coastal precipitation in boreal spring. *Quart. J. Roy. Meteor. Soc.*, **139**, 387–400, <https://doi.org/10.1002/qj.1981>.
- Lélé, M. I., L. M. Leslie, and P. J. Lamb, 2015: Analysis of low-level atmospheric moisture transport associated with the West African monsoon. *J. Climate*, **28**, 4414–4430, <https://doi.org/10.1175/JCLI-D-14-00746.1>.
- Lindzen, R. S., and S. Nigam, 1987: On the role of sea surface temperature gradients in forcing low-level winds and convergence in the tropics. *J. Atmos. Sci.*, **44**, 2418–2436, [https://doi.org/10.1175/1520-0469\(1987\)044<2418:OTROSS>2.0.CO;2](https://doi.org/10.1175/1520-0469(1987)044<2418:OTROSS>2.0.CO;2).
- Losada, T., B. Rodríguez-Fonseca, S. Janicot, S. Gervois, F. Chauvin and P. Ruti, 2010: A multi-model approach to the Atlantic equatorial mode: Impact on the West African monsoon. *Climate Dyn.*, **35**, 29–43, <https://doi.org/10.1007/s00382-009-0625-5>.
- Love, B. S., A. J. Matthews, and G. M. S. Lister, 2011: The diurnal cycle of precipitation over the Maritime Continent in a high-resolution atmospheric model. *Quart. J. Roy. Meteor. Soc.*, **137**, 934–947, <https://doi.org/10.1002/qj.809>.
- Maranan, M., A. H. Fink, and P. Knippertz, 2018: Rainfall types over southern West Africa: Objective identification, climatology and synoptic environment. *Quart. J. Roy. Meteor. Soc.*, **144**, 1628–1648, <https://doi.org/10.1002/qj.3345>.
- Marin, F., G. Caniaux, H. Giordani, B. Bourlès, Y. Gouriou, and E. Key, 2009: Why were sea surface temperatures so different in the eastern equatorial Atlantic in June 2005 and 2006? *J. Phys. Oceanogr.*, **39**, 1416–1431, <https://doi.org/10.1175/2008JPO4030.1>.
- Mekonnen, A., C. D. Thorncroft, and A. R. Aiyer, 2006: Analysis of convection and its association with African easterly waves. *J. Climate*, **19**, 5405–5421, <https://doi.org/10.1175/JCLI3920.1>.
- Meynadier, R., G. de Coëtlogon, M. Leduc-Leballeur, L. Eymard, and S. Janicot, 2015: Seasonal influence of the sea surface temperature on the low atmospheric circulation and precipitation in the eastern equatorial Atlantic. *Climate Dyn.*, **47**, 1127–1142, <https://doi.org/10.1007/s00382-015-2892-7>.
- Myers, T. A., and J. R. Norris, 2013: Observational evidence that enhanced subsidence reduces subtropical marine boundary layer cloudiness. *J. Climate*, **26**, 7507–7524, <https://doi.org/10.1175/JCLI-D-12-00736.1>.
- Nguyen, H., C. D. Thorncroft, and C. Zhang, 2011: Guinean coastal rainfall of the West African monsoon. *Quart. J. Roy. Meteor. Soc.*, **137**, 1828–1840, <https://doi.org/10.1002/qj.867>.
- Nnamchi, H. C., and J. Li, 2011: Influence of the South Atlantic Ocean dipole on West African summer precipitation. *J. Climate*, **24**, 1184–1197, <https://doi.org/10.1175/2010JCLI3668.1>.
- Odekunle, T. O., and A. O. Eludoyin, 2008: Sea surface temperature patterns in the Gulf of Guinea: Their implications for the spatio-temporal variability of precipitation in West

- Africa. *Int. J. Climatol.*, **28**, 1507–1517, <https://doi.org/10.1002/joc.1656>.
- Okumura, Y., and S.-P. Xie, 2004: Interaction of the Atlantic equatorial cold tongue and the African monsoon. *J. Climate*, **17**, 3589–3602, [https://doi.org/10.1175/1520-0442\(2004\)017<3589:IOTAEC>2.0.CO;2](https://doi.org/10.1175/1520-0442(2004)017<3589:IOTAEC>2.0.CO;2).
- Parker, D. J., and Coauthors, 2017: Local weather. *Meteorology of Tropical West Africa: The Forecaster's Handbook*, D. J. Parker and M. Diop-Kane, Eds., John Wiley and Sons, 130–174, <https://doi.org/10.1002/9781118391297.ch4>.
- Peyrillé, P., J.-P. Lafore, and J.-L. Redelsperger, 2007: An idealized two-dimensional framework to study the West African monsoon. Part I: Validation and key controlling factors. *J. Atmos. Sci.*, **64**, 2765–2782, <https://doi.org/10.1175/JAS3919.1>.
- Polo, I., B. Rodríguez-Fonseca, T. Losada, and J. García-Serrano, 2008: Tropical Atlantic variability modes (1979–2002). Part I: Time-evolving SST modes related to West African rainfall. *J. Climate*, **21**, 6457–6475, <https://doi.org/10.1175/2008JCLI2607.1>.
- Pu, B., and K. H. Cook, 2012: Role of the West African westerly jet in Sahel rainfall variations. *J. Climate*, **25**, 2880–2896, <https://doi.org/10.1175/JCLI-D-11-00394.1>.
- Redelsperger, J.-C., C. D. Thorncroft, A. Diedhiou, T. Lebel, D. J. Parker, and J. Polcher, 2006: African Monsoon Multidisciplinary Analysis: An international research project and field campaign. *Bull. Amer. Meteor. Soc.*, **87**, 1739–1746, <https://doi.org/10.1175/BAMS-87-12-1739>.
- Reynolds, R. W., T. M. Smith, C. Liu, D. B. Chelton, K. S. Casey, and M. G. Schlax, 2007: Daily high-resolution-blended analyses for sea surface temperature. *J. Climate*, **20**, 5473–5496, <https://doi.org/10.1175/2007JCLI1824.1>.
- Roehrig, R., D. Bouniol, F. Guichard, F. Hourdin, and J.-L. Redelsperger, 2013: The present and future of the West African monsoon: A process-oriented assessment of CMIP5 simulations along the AMMA transect. *J. Climate*, **26**, 6471–6505, <https://doi.org/10.1175/JCLI-D-12-00505.1>.
- Saha, S., and Coauthors, 2014: The NCEP Climate Forecast System version 2. *J. Climate*, **27**, 2185–2208, <https://doi.org/10.1175/JCLI-D-12-00823.1>.
- Sow, M., M. Diakhaté, R. D. Dixon, F. Guichard, D. Dieng, and A. T. Gaye, 2020: Uncertainties in the annual cycle of rainfall characteristics over West Africa in CMIP5 models. *Atmosphere*, **11**, 216, <https://doi.org/10.3390/atmos11020216>.
- Steinig, S., J. Harlaß, W. Park, and M. Latif, 2018: Sahel rainfall strength and onset improvements due to more realistic Atlantic cold tongue development in a climate model. *Sci. Rep.*, **8**, 2569, <https://doi.org/10.1038/s41598-018-20904-1>.
- Suárez-Moreno, R., B. Rodríguez-Fonseca, J. A. Barroso, and A. H. Fink, 2018: Interdecadal changes in the leading ocean forcing of Sahelian rainfall interannual variability: Atmospheric dynamics and role of multidecadal SST background. *J. Climate*, **31**, 6687–6710, <https://doi.org/10.1175/JCLI-D-17-0367.1>.
- Sultan, B., and S. Janicot, 2003: The West African monsoon dynamics. Part II: The “preonset” and “onset” of the summer monsoon. *J. Climate*, **16**, 3407–3427, [https://doi.org/10.1175/1520-0442\(2003\)016<3407:TWAMDP>2.0.CO;2](https://doi.org/10.1175/1520-0442(2003)016<3407:TWAMDP>2.0.CO;2).
- , —, and P. Drobinski, 2007: Characterization of the diurnal cycle of the West African monsoon around the monsoon onset. *J. Climate*, **20**, 4014–4032, <https://doi.org/10.1175/JCLI4218.1>.
- Sweet, W., R. Fett, J. Kerling, and P. LaViolette, 1981: Air–sea interaction effects in the lower troposphere across the north wall of the Gulf Stream. *Mon. Wea. Rev.*, **109**, 1042–1052, [https://doi.org/10.1175/1520-0493\(1981\)109<1042:ASIEIT>2.0.CO;2](https://doi.org/10.1175/1520-0493(1981)109<1042:ASIEIT>2.0.CO;2).
- Sylla, M. B., I. Diallo, and J. S. Pal, 2013: West African monsoon in state-of-the-science regional climate models. *Climate Variability—Regional and Thematic Patterns*, A. Tarhule, Ed., IntechOpen, 1–35.
- Thorncroft, C. D., H. Nguyen, C. Zhang, and P. Peyrillé, 2011: Annual cycle of the West African monsoon: Regional circulations and associated water vapour transport. *Quart. J. Roy. Meteor. Soc.*, **137**, 129–147, <https://doi.org/10.1002/qj.728>.
- Wainwright, C. M., L. C. Hiron, N. P. Klingaman, R. P. Allan, E. Black, and A. G. Turner, 2019: The impact of air–sea coupling and ocean biases on the seasonal cycle of southern West African precipitation. *Climate Dyn.*, **53**, 7027–7044, <https://doi.org/10.1007/s00382-019-04973-0>.
- Wallace, J. M., 1975: Diurnal variations in precipitation and thunderstorm frequency over the conterminous United States. *Mon. Wea. Rev.*, **103**, 406–419, [https://doi.org/10.1175/1520-0493\(1975\)103<0406:DVIPAT>2.0.CO;2](https://doi.org/10.1175/1520-0493(1975)103<0406:DVIPAT>2.0.CO;2).
- , T. P. Mitchell, and C. Deser, 1989: The influence of sea-surface temperature on surface wind in the eastern equatorial Pacific: Seasonal and interannual variability. *J. Climate*, **2**, 1492–1499, [https://doi.org/10.1175/1520-0442\(1989\)002<1492:TIOSSST>2.0.CO;2](https://doi.org/10.1175/1520-0442(1989)002<1492:TIOSSST>2.0.CO;2).
- Wang, G., and E. A. B. Eltahir, 2000: Role of vegetation dynamics in enhancing the low-frequency variability of the Sahel rainfall. *Water Resour. Res.*, **36**, 1013–1021, <https://doi.org/10.1029/1999WR900361>.
- Weller, E., K. Shelton, M. J. Reeder, and C. Jakob, 2017: Precipitation associated with convergence lines. *J. Climate*, **30**, 3169–3183, <https://doi.org/10.1175/JCLI-D-16-0535.1>.
- Worou, K., H. Goosse, T. Fichet, F. Guichard, and M. Diakhaté, 2020: Interannual variability of rainfall in the Guinean coast region and its links with sea surface temperature changes over the twentieth century for the different seasons. *Climate Dyn.*, **55**, 449–470, <https://doi.org/10.1007/s00382-020-05276-5>.
- Yang, G.-Y., and J. Slingo, 2001: The diurnal cycle in the tropics. *Mon. Wea. Rev.*, **129**, 784–801, [https://doi.org/10.1175/1520-0493\(2001\)129<0784:TDCITT>2.0.CO;2](https://doi.org/10.1175/1520-0493(2001)129<0784:TDCITT>2.0.CO;2).
- Zhang, G., and K. H. Cook, 2014: West African monsoon demise: Climatology, interannual variations, and relationship to seasonal rainfall. *J. Geophys. Res. Atmos.*, **119**, 10 175–10 193, <https://doi.org/10.1002/2014JD022043>.
- Zheng, X., E. A. B. Eltahir, and K. A. Emanuel, 1999: A mechanism relating tropical Atlantic spring sea surface temperature and West African rainfall. *Quart. J. Roy. Meteor. Soc.*, **125**, 1129–1163, <https://doi.org/10.1002/qj.1999.49712555604>.